Corrosion Fatigue of Alloys 600 and 690 in Simulated LWR Environments

Prepared by
W. E. Ruther, W. K. Soppet, T. F. Kassner

Argonne National Laboratory

MASTER

Corrosion Fatigue of Alloys 600 and 690 in Simulated LWR Environments

Prepared by
W. E. Ruther, W. K. Soppett, T. F. Kassner

Argonne National Laboratory
9700 South Cass Avenue
Argonne, IL 60439

M. McNeil, NRC Project Manager

Corrosion Fatigue of Alloys 600 and 690 in Simulated LWR Environments

by

W. E. Ruther, W. K. Soppet, and T. F. Kassner

Abstract

Crack growth data were obtained on fracture–mechanics specimens of Alloys 600 and 690 to investigate environmentally assisted cracking (EAC) in simulated boiling water reactor and pressurized water reactor environments at 289 and 320°C. Preliminary information was obtained on the effect of temperature, load ratio, stress intensity (K), and the dissolved–oxygen and –hydrogen concentrations of the water on EAC. Specimens of Type 316NG and sensitized Type 304 stainless steel (SS) were included in several of the experiments to assess the behavior of these materials and Alloy 600 under the same water chemistry and loading conditions. The experimental data are compared with predictions from an Argonne National Laboratory (ANL) model for crack growth rates (CGRs) of SSs in water and the ASME Code Section XI correlation for CGRs in air at the K_{max} and load–ratio values in the various tests. The data for all of the materials were bounded by ANL model predictions and the ASME Section XI "air line."

Contents

Figures

Tables

Executive Summary

Fracture-mechanics crack growth rate (CGR) tests were conducted on compact–tension specimens of mill–annealed Alloy 600 and thermally treated Alloy 690 in oxygenated water and in deaerated water that contained boron, lithium, and low concentrations of dissolved hydrogen at 289 and 320°C. Specimens of sensitized Type 304 and Type 316NG stainless steel (SS) were included in several experiments to compare the behavior of these materials with that of Alloy 600 under the same water chemistry and loading conditions. The experimental data are compared with predictions from an Argonne National Laboratory (ANL) model for CGRs of SSs in water and the ASME Code Section XI correlation for CGRs in air at the maximum stress intensity (K_{max}) and load–ratio R values in the various tests. The data for all of the materials were bounded by ANL model predictions and by the ASME "air line."

Comparison of CGRs of Sensitized Type 304 SS and Mill–Annealed Alloy 600 in Oxygenated Water

The effect of water chemistry on CGRs of mill–annealed Alloy 600 and sensitized Type 304 SS was explored at a load ratio of 0.95. Small amounts of chromate and sulfate (<200 ppb) and two amines (1–5 ppm) in water that contained ≈200 ppb dissolved oxygen (DO) produced small but measurable changes in the CGRs of the sensitized Type 304 SS specimens but had virtually no effect on the CGR of the Alloy 600 specimen. The average CGR of the Alloy 600 and sensitized Type 304 SS specimens was ≈2.3 x 10^{-10} m·s^{-1} at aload ratio of 0.95 and K_{max} of >30 MPa·m$^{1/2}$ under these water chemistry conditions. This rate is consistent with CGRs of sensitized Type 304 and nonsensitized Type 316NG SS specimens in oxygenated water at 289°C under similar loading conditions. The observation that different materials, e.g., Alloy 600, sensitized Type 304, nonsensitized Type 316NG, and Grade CF–3, CF–8, and CF–8M cast SS, exhibit approximately the same CGR in oxygenated water despite significant differences in material chemistry, microstructure, and mode of crack propagation, suggests that crack propagation is largely controlled by the rate of cathodic reduction of DO with a concomitant anodic dissolution process at the crack tip.

Comparison of CGRs of Mill–Annealed Alloy 600, Sensitized Type 304 SS, and Type 316NG SS in Oxygenated Water and in Simulated PWR Water

Experiments were also performed in simulated pressurized water reactor (PWR) primary–system water that contained 450 ppm B and 2.25 ppm Li (added to the feedwater as H_3BO_3 and LiOH), 3–58 cm^3 H_2·kg^{-1} H_2O, ≈1 ppb DO, and 750 ppb hydrazine. Hydrazine was added to the feedwater to scavenge residual DO to a very low level. In these experiments, the role of H_3BO_3, LiOH, and dissolved hydrogen in crack growth was investigated vis–a`–vis high–purity (HP) deoxygenated water. Experimental CGR data for Alloy 600 and Type 304 and 316NG SS specimens in simulated PWR primary–system water were also compared with rates for wrought SSs in air from the ASME Code Section XI correlation and the ANL model that was modified to assess crack growth in low–oxygen environments with no contribution from stress corrosion cracking. With the exception of one data point for an Alloy 600 specimen, the experimental results are bounded by the ANL model prediction and by the air curve for austenitic SSs predicted by the ASME Code.

CGRs of Mill–Annealed Alloy 600 and Thermally Treated Alloy 690 in HP Water at 289 and 320°C

Corrosion–fatigue experiments were conducted on mill–annealed Alloy 600 and mill–annealed plus thermally treated Alloy 690 specimens in HP water to investigate the effects of temperature, DO, and dissolved hydrogen in water on CGRs of these materials. Initial results were obtained at 289°C in water that contained $\approx$6–8 ppm and <5 ppb DO, load ratios of 0.2, 0.6, and 0.9, and K_{max} of 31–33 MPa·m$^{1/2}$. Crack growth behavior of the two materials is quite similar under the conditions in these experiments. In water that contained <5 ppb DO, CGRs at 289 and 320°C were similar. At a load ratio of 0.6, CGRs are not dependent on DO, which is indicative of a strong contribution of cyclic loading to the rates. At a higher load ratio of 0.9, CGRs decreased as DO concentration decreased at 289 and 320°C. In all cases, CGRs of both materials were near or below the "air" curve for austenitic SSs.

Several tests were conducted at 320°C in HP water that contained <5 ppb DO and $\approx$0, 2.2 and 53 cm^3·kg^{-1} dissolved hydrogen. At a load ratio of 0.9, CGRs of both specimens were low (0.5–1.3 x 10^{-11} m·s^{-1}) and dissolved hydrogen over the range of $\approx$2–53 cm^3 H$_2$·kg^{-1} H$_2$O did not influence the rates at a K_{max} of $\approx$34 MPa·m$^{1/2}$. In contrast to results at lower load ratios (i.e., ≤0.6), CGRs of Alloy 600 were greater than those of Alloy 690 by factors of $\approx$2–5.

CGRs of Mill–Annealed Alloy 600 and Thermally Treated Alloy 690 in Simulated PWR Water at 289 and 320°C

The influence of dissolved hydrogen in simulated PWR water on CGRs of Alloy 600 and 690 specimens at 289 and 320°C was determined in another series of experiments. The water contained 450 ppm B, 2.25 ppm Li, <2 ppb DO, and $\approx$3–58 cm^3 H$_2$·kg^{-1} H$_2$O. Tests were conducted at a load ratio of 0.8 and K_{max} in the range of $\approx$30–41 MPa·m$^{1/2}$. CGRs decreased slightly as dissolved hydrogen concentration was increased from 3 to 58 cm^3·kg^{-1}. At both temperatures, and under these water chemistry and loading conditions, the CGR of Alloy 690 was higher by a factor of $\approx$3 than the CGR of Alloy 600.

CGRs decrease significantly as load ratio increases in both HP and simulated PWR water environments. At load ratios ≤0.8, it appears that CGRs of the Alloy 690 specimens are slightly higher than those of Alloy 600; however, at a load ratio of 0.9 the CGRs of the alloys are similar. Crack growth experiments will be conducted at higher load ratios, including constant load (R = 1.0), to determine whether Alloy 690 exhibits lower rates than Alloy 600 at higher R values.

Acknowledgments

1 Introduction

The objective of this work is to evaluate and compare the resistance of Alloys 600 and 690 to environmentally assisted cracking (EAC) in simulated light water reactor (LWR) coolant environments. High–nickel alloys have experienced general corrosion (tube wall thinning), localized intergranular attack (IGA), and stress corrosion cracking (SCC) in LWRs. Secondary–side IGA[*] and axial and circumferential SCC[**] have occurred in Alloy 600 tubes at tube support plates in many steam generators. Primary–water stress corrosion cracking (PWSCC) of Alloy 600 steam generator tubes in pressurized water reactors (PWRs) at roll transitions and U–bends and in tube plugs[***] is a widespread problem that has been studied intensively. Cracking has also occurred in Alloy 600 and other high–nickel alloys (e.g., Inconel–82 and –182 and Alloy X750) that are used in applications such as (a) instrument nozzles and heater thermal sleeves in the pressurizer[†] and penetrations for control–rod drive mechanisms in reactor vessel closure heads in the primary system of PWRs[††] and (b) in dissimilar–metal welds between SS piping and low–alloy steel nozzles, in jet pump hold–down beams,[†††] and in shroud–support–access–hole covers[§] in boiling water reactors (BWRs). Alloy 600, in general, undergoes different thermomechanical processing for applications other than those used for steam generator tubes. Because environmental degradation of the alloys in many cases is very sensitive to processing, further evaluation of even SCC is needed. In addition, experience strongly suggests that materials that are susceptible to SCC are also susceptible to environmental degradation of fatigue life and fatigue–crack growth properties.

In this investigation, we have obtained preliminary information on the effect of temperature, load ratio R, and stress intensity (K) on EAC of Alloys 600 and 690 in simulated BWR and PWR water. Crack growth rates (CGRs) of these materials have been compared with those of Type 316NG and sensitized Type 304 SS under conditions where EAC occurs in all of the materials.

---

[*] USNRC Information Notice No. 91–67, "Problems with the Reliable Detection of Intergranular Attack (IGA) of Steam Generator Tubing," October 1991.

[**] USNRC Information Notice No. 90–49, "Stress Corrosion Cracking in PWR Steam Generator Tubes," August 1990; Notice No. 91–43, "Recent Incidents Involving Rapid Increases in Primary–to–Secondary Leak Rate," July 1991; Notice No. 92–80, "Operation with Steam Generator Tubes Seriously Degraded," December 1992; Notice No. 94–05, "Potential Failure of Steam Generator Tubes with Kinetically Welded Sleeves," January 1994.

[***] USNRC Information Notice No. 89–33, "Potential Failure of Westinghouse Steam Generator Tube Mechanical Plugs," March 1989; Notice No. 89–65, "Potential for Stress Corrosion Cracking in Steam Generator Tube Plugs Supplied by Babcock and Wilcox," September 1989; Notice No. 94–87, "Unanticipated Crack in a Particular Heat of Alloy 600 Used for Westinghouse Mechanical Plugs for Steam Generator Tubes," December 1994.

[†] USNRC Information Notice No. 90–10, "Primary Water Stress Corrosion Cracking (PWSCC) of Inconel 600," February 1990.

[††] INPO Document SER 20–93 "Intergranular Stress Corrosion Cracking of Control Rod Drive Mechanism Penetrations," September 1993.

[†††] USNRC Information Notice No. 93–101, "Jet Pump Hold–Down Beam Failure," December 1993.

[§] USNRC Information Notice No. 92–57, "Radial Cracking of Shroud Support Access Hole Cover Welds," August 1992.

2 Material Characterization

The various heats of Alloys 600 and 690 that were obtained for corrosion–fatigue testing were characterized. The heat identification numbers, product form, and source of materials for fabrication of 1T compact tension (1TCT) specimens are given in Table 1.

Table 1. Product form and source of Alloys 600 and 690

Material	Heat No.	Material Condition	Product Form	Source
600	NX8844B–33	Annealed 872°C/1 h	1.0–in.–thick plate	EPRI[a]
600	J422	Mill Annealed	1T–CT specimens	Metal Samples Co.
600	NX8197	Mill Annealed	1.0–in.–thick plate	A. M. Castle & Co.
600	NX8844J–26	Annealed 1038°C/1 h	1.0–in.–thick plate	EPRI
600	NX8844G–3	Hot Worked 982°C, 20% Reduction	1.0–in.–thick plate	EPRI
690	NX8662HG–33	Annealed + 715°C/5 h	1.34–in.–thick plate	INCO Alloys Intl., Inc.
690	NX8625HG–21	Annealed + 715°C/5 h	1.34–in.–thick plate	EPRI
690	NX8244HK–1A	Annealed 982°C/1 h	1.0–in.–thick plate	EPRI
690	NX8244HK–1B	Annealed 1093°C/1 h	1.0–in.–thick plate	EPRI

[a]Numerous heats of Alloys 600 and 690 were fabricated by INCO Alloys International, Inc., Huntington, WV, for the Electric Power Research Institute (EPRI), Palo Alto, CA, which provided materials for this study.

The composition of the materials is given in Tables 2 and 3. The tensile properties of cylindrical specimens in air at 25, 290, and 320°C and at a strain rate of 1.0×10^{-4} s^{-1} were determined in accordance with ASTM Standard E8. Vickers hardness was measured at room temperature, and average grain size of the various heats of Alloys 600 and 690 was determined by following the procedure in ASTM Standard E112. The results for Alloys 600 and 690 are given in Tables 4 and 5, respectively. Properties obtained from certified material test reports (CMTRs) supplied by the vendors or documentation obtained from the EPRI are also included in Tables 4 and 5. Data for annealed specimens tend to follow a Petch relationship, i.e., $\sigma_y = \sigma_i + k \cdot d^{-1/2}$, where σ_y is the yield stress; d, the grain diameter; k, an emperical constant; and σ_i, the "friction" stress, which is a measure of intrinsic resistance of the material to dislocation motion. The dependence of the yield stress of annealed Alloy 600 (Heat NX8844) and 690 (Heat NX8244HK) specimens on average grain size at 25, 290, and 320°C is shown in Fig. 1. The relationship between ASTM grain size and average grain diameter is shown in Fig. 2. Photomicrographs that were used to determine the grain size of the various heats of Alloys 600 and 690 are shown in Figs. 3 and 4, respectively.

A small section of each material was used to prepare metallographic specimens to qualitatively determine the degree of grain boundary carbide coverage by optical metallography. Specimens were polished to a 0.25–µm diamond finish with Struers DP–Spray, and a Vickers hardness indentation was made to provide a reference point for subsequent examination to reveal the carbide distribution and grain boundaries after two chemical etching methods. The specimens were electroetched in a 10% H_3PO_4 solution at ≈10 V for ≈25 s, rinsed in ethanol, and air dried. Photomicrographs obtained at 500X magnification reveal

Table 2. Composition of Alloy 600 heats used for corrosion fatigue tests

Material	Heat No.	Analysis	Composition (wt.%)															
			Cr	Mo	Ni	Fe	Mn	Si	C	N	P	S	B	Cu	Ti	Al	Co	Nb+Ta
Alloy 600	J422	Vendor	15.36	–	75.72	7.51	0.21	0.32	0.080	–	0.008	<0.001	–	0.15	0.24	0.28	0.05	0.07
		ANL	15.37	0.23	76.36	7.27	0.20	0.32	0.080	0.0145	0.016	0.004	0.002	0.15	0.16	0.27	0.05	0.06
Alloy 600	NX8197	Vendor	15.88	–	75.05	7.76	0.22	0.23	0.080	–	0.006	0.002	–	0.12	0.27	0.26	0.05	0.07
		ANL	15.43	0.58	73.82	9.20	0.20	0.27	0.080	0.0099	0.016	0.002	0.002	0.11	0.18	0.24	0.06	0.05
Alloy 600	NX8844	Vendor	14.97	0.15	75.21	8.26	0.26	0.24	0.069	0.01	0.009	<0.001	0.004	0.22	0.29	0.27	0.04	–
	NX8844B-33	ANL	15.03	0.17	75.16	7.93	0.24	0.27	0.080	0.0146	0.019	0.001	0.003	0.22	0.21	0.28	0.04	0.04
	NX8844J-26	ANL	15.00	0.16	74.94	8.14	0.23	0.32	0.060	0.0155	0.014	0.002	0.004	0.22	0.24	0.24	0.03	0.03
	NX8844G-3	ANL	15.14	0.16	74.78	8.28	0.23	0.35	0.070	0.0145	0.015	0.002	0.005	0.22	0.25	0.25	0.04	0.04

Table 3. Composition of Alloy 690 heats used for corrosion fatigue tests

Material	Heat No.	Analysis	Composition (wt.%)															
			Cr	Mo	Ni	Fe	Mn	Si	C	N	P	S	B	Cu	Ti	Al	Co	Nb+Ta
Alloy 690	NX8662HG-33	Vendor	30.25	–	59.31	9.54	0.10	0.16	0.030	0.050	0.008	<0.001	0.004	0.04	0.28	0.33	0.022	–
		ANL	30.46	0.04	58.88	9.22	0.11	0.16	0.030	0.047	0.017	0.001	0.003	0.05	0.25	0.32	0.020	0.01
Alloy 690	NX8625HG-21	Vendor	30.28	–	58.56	10.00	0.11	0.26	0.027	0.030	0.009	<0.001	0.004	0.06	0.32	0.44	0.036	–
		ANL	30.64	0.02	58.10	9.84	0.12	0.32	0.030	0.029	0.009	0.002	0.004	0.01	0.28	0.39	0.030	<0.01
Alloy 690	NX8244HK	Vendor	30.03	–	59.85	9.20	0.20	0.14	0.018	0.01	0.004	<0.001	0.002	<0.01	0.20	0.36	0.003	–
	NX8244HK-1A	ANL	30.66	<0.01	59.09	9.22	0.20	0.18	0.024	0.010	0.004	0.002	0.002	<0.01	0.20	0.31	<0.01	<0.01
	NX8244HK-1B	ANL	30.64	<0.01	59.20	9.19	0.21	0.18	0.023	0.011	0.005	0.002	0.002	<0.01	0.19	0.32	<0.01	<0.01

Table 4. Tensile properties of Alloy 600 under various heat treatment conditions

Alloy 600 Heat No.	Material Condition	Test No.	Spec. No.	Temp., °C	σ_u, MPa	σ_y, MPa	ε_t, %	RA, %	Hardness, VN	Hardness,[a] R_b	ASTM Grain Size
NX8844B-33	Annealed 872°C/1 h	–[b]	–[b]	25	748.8	339.9	35.5	–	–	90	7.5
NX8844B-33	Annealed 872°C/1 h	T19	B33–05	25	714.9	333.2	39.6	66.9	91	–	8
NX8844B-33	Annealed 872°C/1 h	T8	B33–03[c]	290	686.1	282.6	38.6	61.1	–	–	–
NX8844B-33	Annealed 872°C/1 h	T10	B33–04[c]	320	680.6	282.6	39.1	55.5	–	–	–
J422	Mill Annealed	–[b]	–[b]	25	722.6	273.0	40.0	–	–	87	–
J422	Mill Annealed	T20	IN–05[c]	25	732.8	370.7	39.2	64.5	93	–	7
J422	Mill Annealed	T9	IN–03[c]	290	699.4	313.7	40.1	53.5	–	–	–
J422	Mill Annealed	T11	IN–04[c]	320	697.9	311.3	39.0	53.9	–	–	–
NX8197	Mill Annealed	–[b]	–[b]	25	683.3	256.5	42.0	–	–	81	–
NX8197	Mill Annealed	T7	197–04[c]	25	683.9	373.6	42.2	64.4	90	–	6
NX8197	Mill Annealed	T12	197–05[c]	25	685.4	392.8	41.6	64.9	–	–	–
NX8197	Mill Annealed	T3	197–02[c]	290	668.1	316.9	46.8	62.2	–	–	–
NX8197	Mill Annealed	T5	197–03[c]	320	656.8	327.4	42.4	60.5	–	–	–
NX8844J-26	Annealed 1038°C/1 h	–[b]	–[b]	25	694.3	298.6	41.0	–	–	86	4
NX8844J-26	Annealed 1038°C/1 h	T21	J26–05	25	653.5	245.5	49.2	61.1	87	–	4
NX8844J-26	Annealed 1038°C/1 h	T23	J26–06	290	637.8	234.0	45.2	53.3	–	–	–
NX8844J-26	Annealed 1038°C/1 h	T25	J26–07	320	639.4	246.8	45.8	48.9	–	–	–
NX8844G-3	Hot Worked 982°C, 20% Reduction	–[b]	–[b]	25	697.8	355.1	38.5	–	–	85	2.5
NX8844G-3	Hot Worked 982°C, 20% Reduction	T13	G3–05[c]	25	666.4	335.3	43.5	56.9	90	–	2
NX8844G-3	Hot Worked 982°C, 20% Reduction	T15	G3–06[c]	290	630.1	292.2	44.1	53.5	–	–	–
NX8844G-3	Hot Worked 982°C, 20% Reduction	T17	G3–07[c]	320	630.3	297.0	44.9	54.9	–	–	–

[a]Vickers hardness at room temperature, 500 gf, 15 s.
[b]Results from vendor (EPRI document or CMTRs).
[c]Tensile tests conducted in air at a strain rate of 1.0×10^{-4} s^{-1}.

4

Table 5. Tensile properties of Alloy 690 under various heat treatment conditions

Alloy 690 Heat No.	Material Condition	Test No.	Spec. No.	Temp., °C	σ_u, MPa	σ_y, MPa	ε_r, %	RA, %	Hardness,[a] VN	Hardness. R_b	ASTM Grain Size
NX8662HG–33	Annealed + 715°C/5 h	_b	_b	25	670.2	291.7	43.5	–	–	82	5
NX8662HG–33	Annealed + 715°C/5 h	T6	HG–03c	25	683.8	292.1	48.7	63.2	96	–	5
NX8662HG–33	Annealed + 715°C/5 h	T2	HG–01c	290	601.2	237.1	49.7	61.6	–	–	–
NX8662HG–33	Annealed + 715°C/5 h	T4	HG–02c	320	598.8	232.3	50.7	62.8	–	–	–
NX8625HG–21	Annealed + 715°C/5 h	_b	_b	25	660.5	268.9	48.0	–	–	82	4
NX8625HG–21	Annealed + 715°C/5 h	T27	G21–03c	25	641.8	297.0	56.4	75.2	86	–	5
NX8625HG–21	Annealed + 715°C/5 h	T28	G21–04c	290	570.9	225.2	56.0	58.8	–	–	–
NX8625HG–21	Annealed + 715°C/5 h	T29	G21–06c	320	567.8	220.4	56.9	61.3	–	–	–
NX8244HK–1A	Annealed 982°C/1 h	_b	_b	25	665.0	245.2	51.0	–	–	78	–
NX8244HK–1A	Annealed 982°C/1 h	T14	K1A–03c	25	647.7	256.3	56.9	75.2	82	–	5
NX8244HK–1A	Annealed 982°C/1 h	T16	K1A–04c	290	569.8	195.4	58.5	71.8	–	–	–
NX8244HK–1A	Annealed 982°C/1 h	T18	K1A–05c	320	572.2	196.4	58.2	71.7	–	–	–
NX8244HK–1B	Annealed 1093°C/1 h	_b	_b	25	602.8	212.3	59.0	–	–	70	–
NX8244HK–1B	Annealed 1093°C/1 h	T22	K1B–05c	25	592.2	215.6	70.5	71.6	80	–	2
NX8244HK–1B	Annealed 1093°C/1 h	T24	K1B–06c	290	504.9	145.2	70.6	68.1	–	–	–
NX8244HK–1B	Annealed 1093°C/1 h	T26	K1B–07c	320	499.4	150.9	67.1	67.3	–	–	–

[a]Vickers hardness at room temperature, 500 gf, 15 s.
bResults from vendor (EPRI document).
cTensile tests conducted in air at a strain rate of 1.0×10^{-4} s^{-1}.
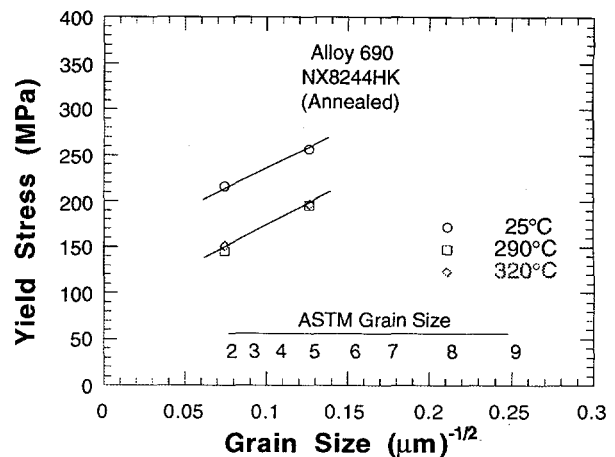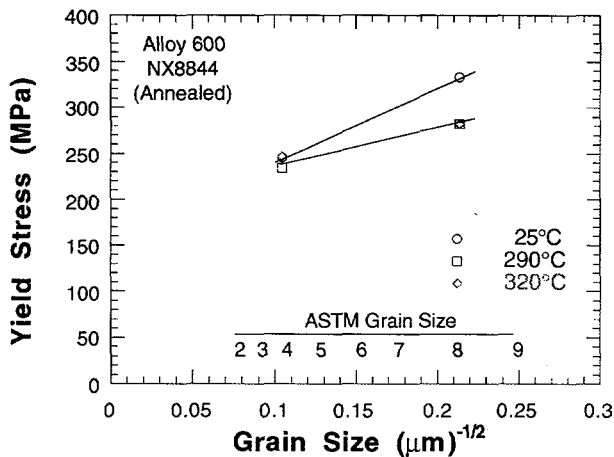
Figure 1. Dependence of 0.2% yield stress at 25, 290, and 320°C on grain size of annealed Alloy 600 and 690 specimens
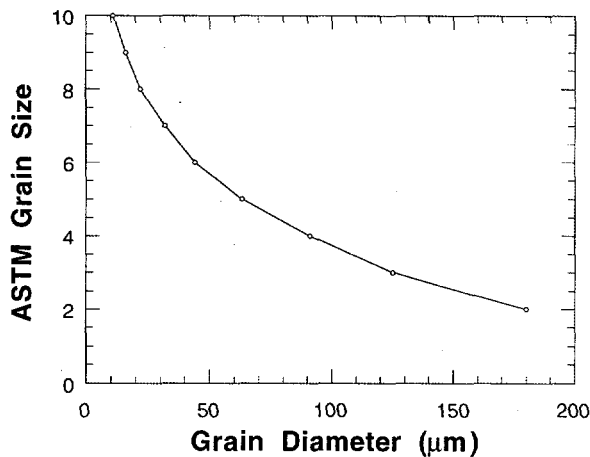
Figure 2.
Relationship between ASTM grain size and average grain diameter

that carbides were the predominant phase present in the specimens. The specimens were repolished with 1.0 and 0.25–μm diamond spray, electroetched in a 5% nital solution (5 mL of HNO_3 in 100 mL ethanol) at ≈10 V for ≈35 s, rinsed in ethanol, and air dried. The same locations on the specimens were photographed once again at a magnification of 500X, with the aid of the hardness indentation, to better reveal grain boundaries and obtain a qualitative estimate of the extent of carbide precipitation thereon.

Photomicrographs of the five heats of Alloy 600 (≈0.06 wt.% carbon) in Figs. 5–9 indicate either semicontinuous or continuous carbide precipitation at the grain boundaries and a significant amount of intragranular carbide. Photomicrographs of the four heats of Alloy 690 (≈0.03 wt.% carbon) in Figs. 10–13 reveal continuous precipitation of carbides at the grain boundaries, with relatively few intragranular carbides. The precipitate phases present in Alloys 600 and 690 are Cr–rich M_7C_3 and $M_{23}C_6$ carbides and Ti(C,N) carbonitrides.[1-3] In general, the microstructures are consistent with the thermomechanical processing histories and carbon concentrations vis–a`–vis the solubility of carbon in the materials (Fig. 14).[4] Namely, according to these carbon solubility data, none of the materials was annealed at a temperature high enough to dissolve all of the carbon in the grain matrix (Alloy 690, >1200°C and Alloy 600, >1080°C); consequently, carbides are present on grain boundaries as well as within the grains, in particular, Alloy 600, which contains ≈0.06 wt.% carbon.
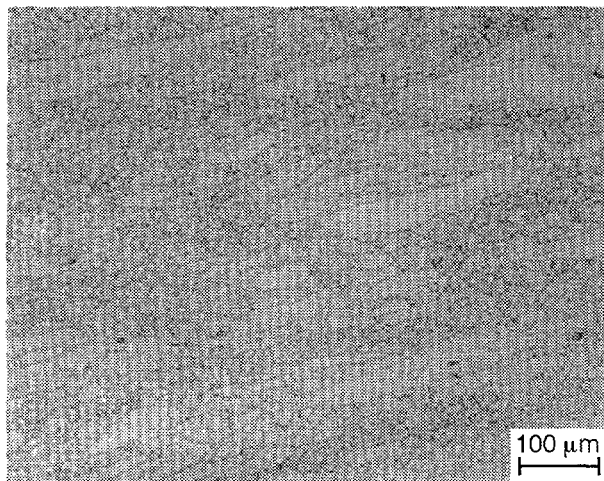
(a) Heat NX8844B–33, annealed at 872°C for 1 h, ASTM grain size 8
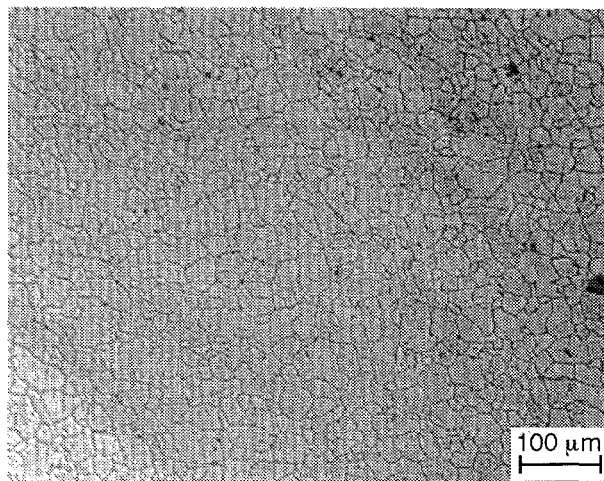
(b) Heat J422, mill annealed, ASTM grain size 7
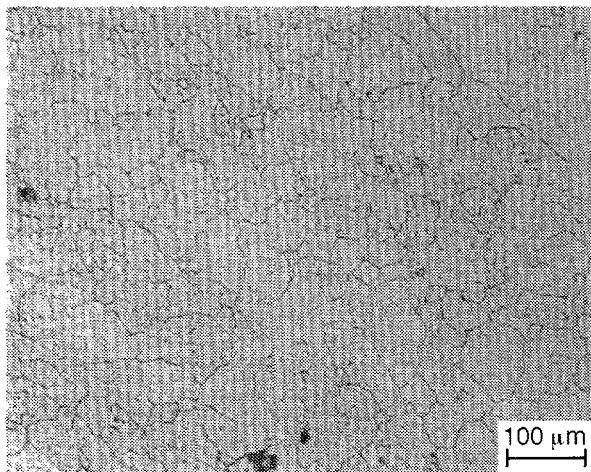
(c) Heat NX8197, mill annealed, ASTM grain size 6
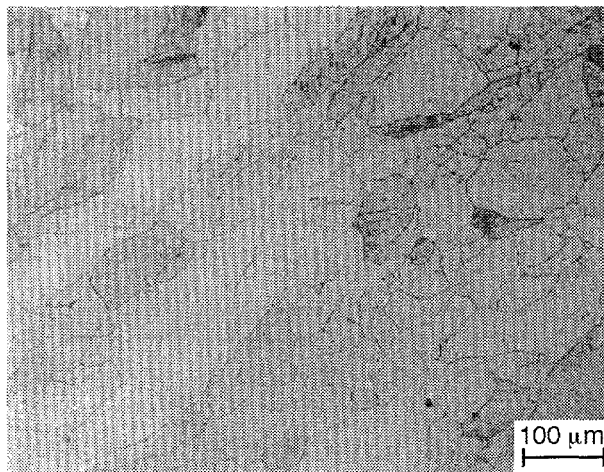
(d) Heat NX8844J–26, annealed at 1038°C for 1 h, ASTM grain size 4
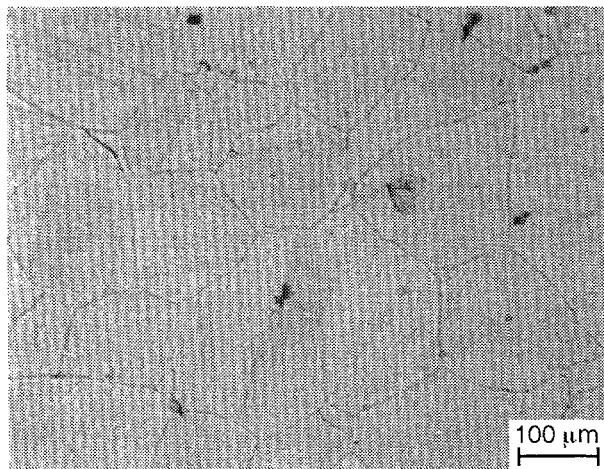
(e) NX8844G–3, hot worked at 982°C 20% reduction, ASTM grain size 2

Figure 3.   Photomicrographs used to determine grain size of various heats of Alloy 600
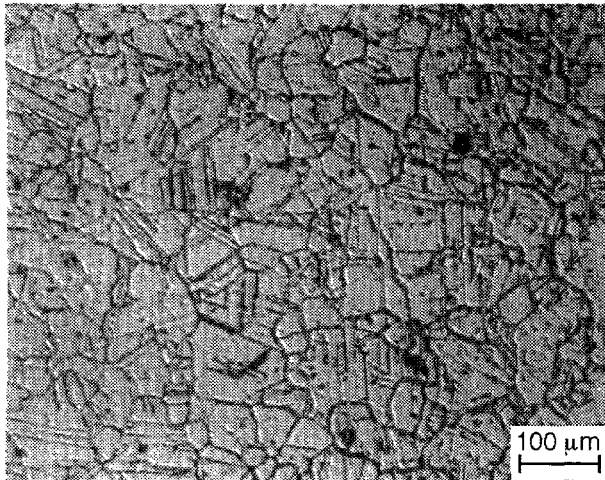
(a) Heat NX8662HG–33, annealed and thermally treated at 715°C for 5 h, ASTM grain size 5
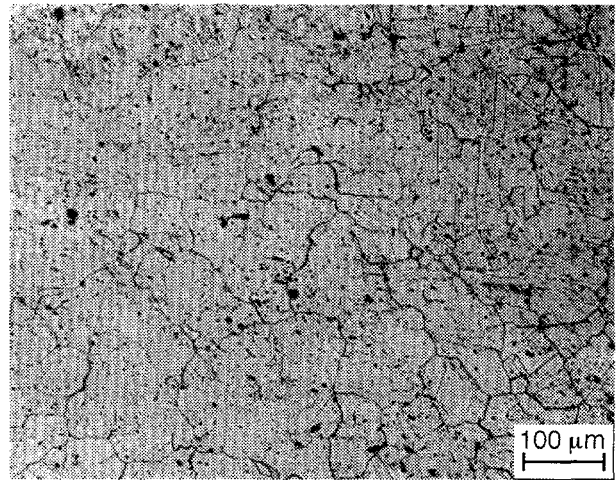
(b) Heat NX8625HG–21, annealed and thermally treated at 715°C for 5 h, ASTM grain size 5
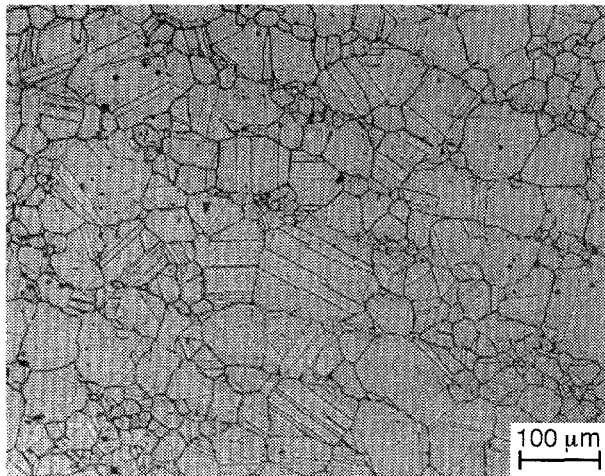
(c) Heat NX8244HK–1A, annealed at 982°C for 1 h, ASTM grain size 5
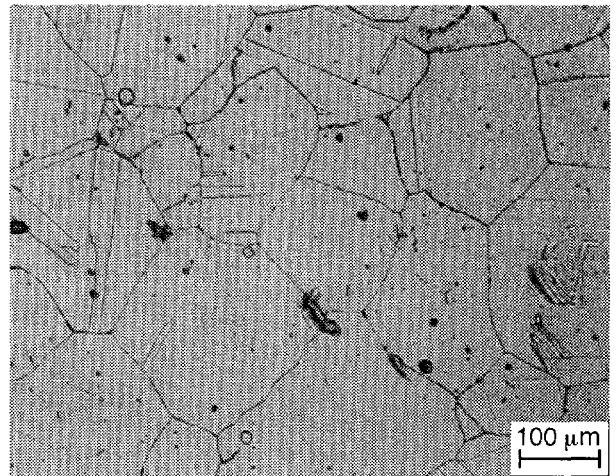
(d) Heat NX8244HK–1B, annealed at 1093°C for 1 h, ASTM grain size 2

Figure 4.   Photomicrographs used to determine grain size of various heats of Alloy 690
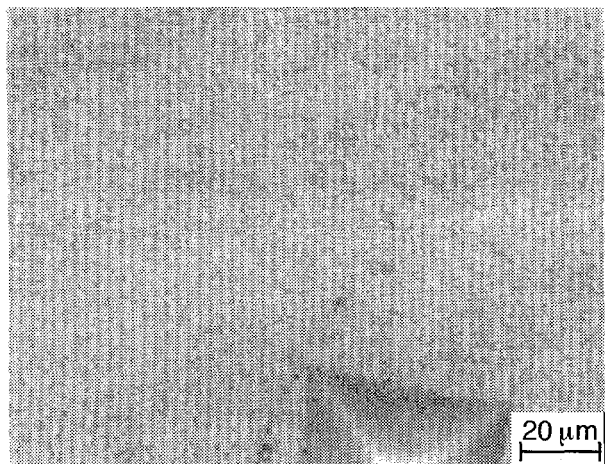
(a) Electroetched in 10% phosphoric acid solution
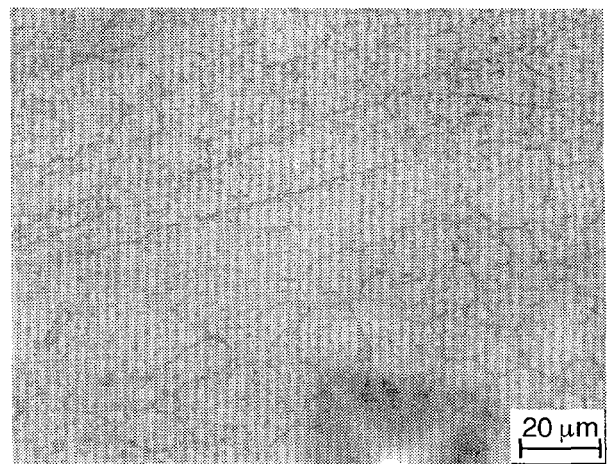
(b) Repolished and electroetched in 5% nital solution

Figure 5.   Microstructures of Alloy 600, Heat NX8844B–33, that show a uniform distribution of intergranular and intragranular carbides
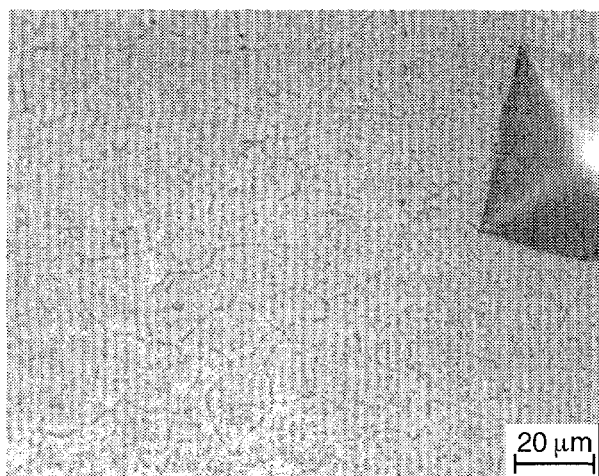
(a) Electroetched in 10% phosphoric acid solution
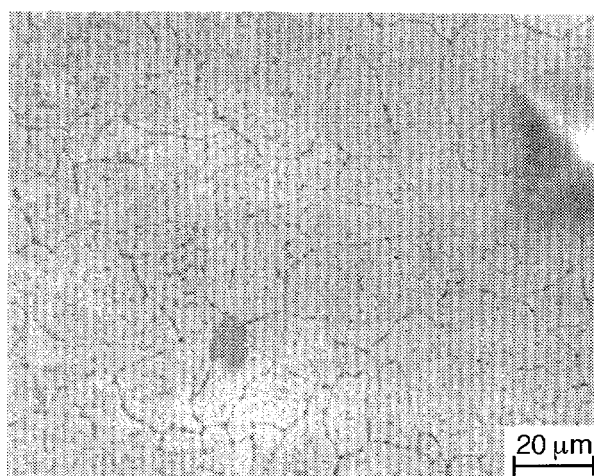
(b) Repolished and electroetched in 5% nital solution

Figure 6. Microstructures of Alloy 600, Heat J422, that show semicontinuous intergranular and intragranular carbides
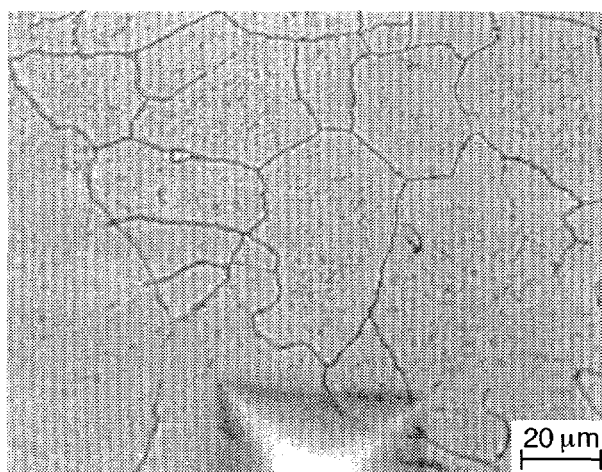
(a) Electroetched in 10% phosphoric acid solution
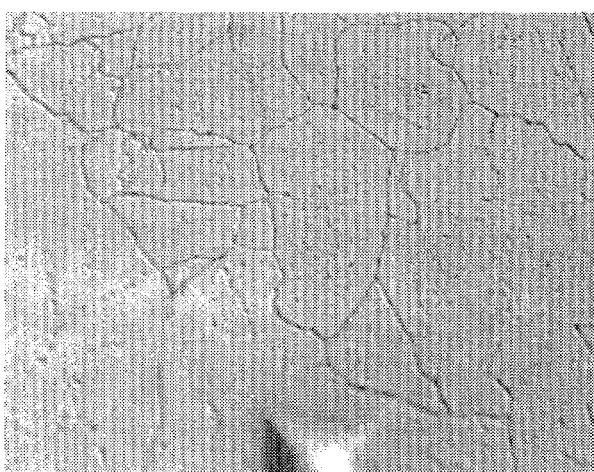
(b) Repolished and electroetched in 5% nital solution

Figure 7. Microstructures of Alloy 600, Heat NX8197, that show continuous intergranular and intragranular carbides
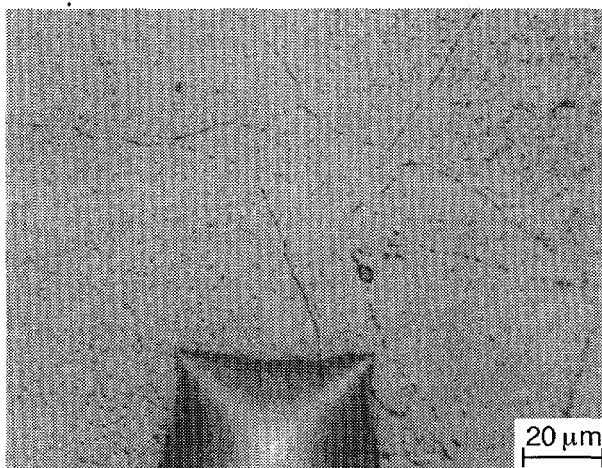
(a) Electroetched in 10% phosphoric acid solution
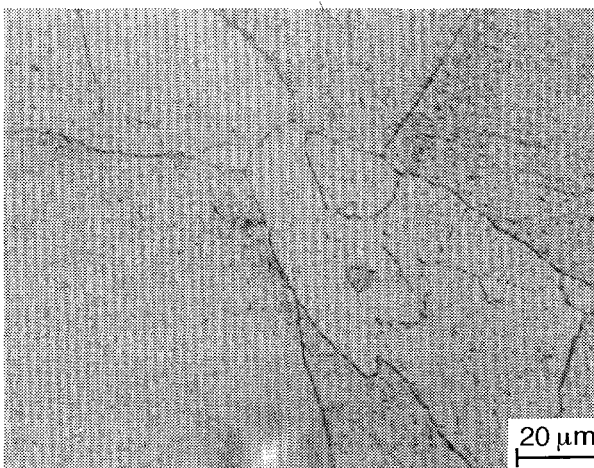
(b) Repolished and electroetched in 5% nital solution

Figure 8. Microstructures of Alloy 600, Heat NX8844J-26, that show semicontinuous intergranular and intragranular carbides
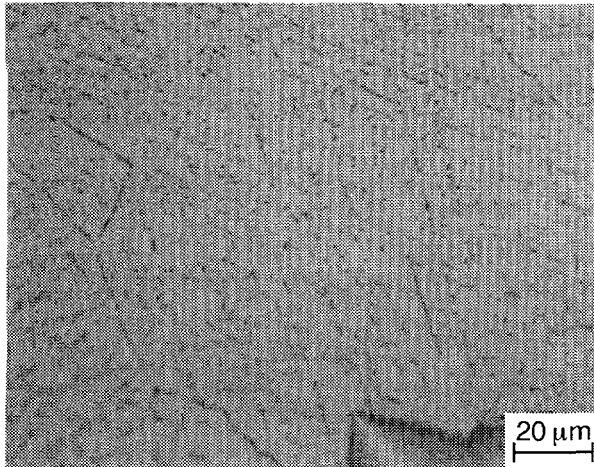
9
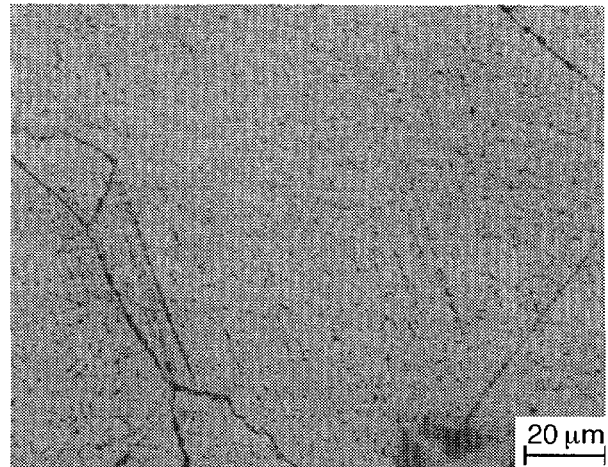
(a) Electroetched in 10% phosphoric acid solution (b) Repolished and electroetched in 5% nital solution

Figure 9. Microstructures of Alloy 600, Heat NX8844G–3, that show semicontinuous intergranular and intragranular carbides along slip lines
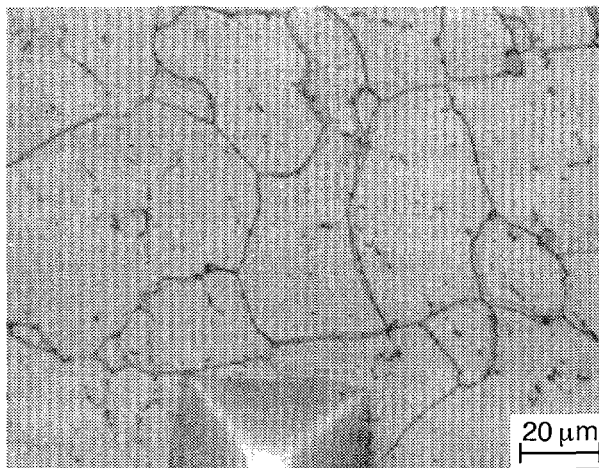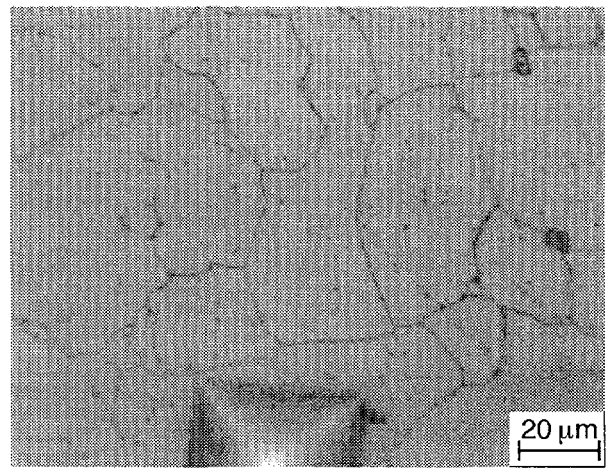
(a) Electroetched in 10% phosphoric acid solution (b) Repolished and electroetched in 5% nital solution

Figure 10. Microstructures of Alloy 690, Heat NX8662HG–33, that show continuous intergranular and relatively few intragranular carbides
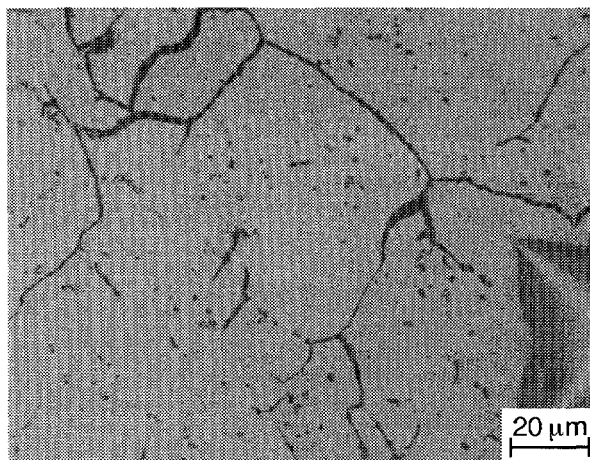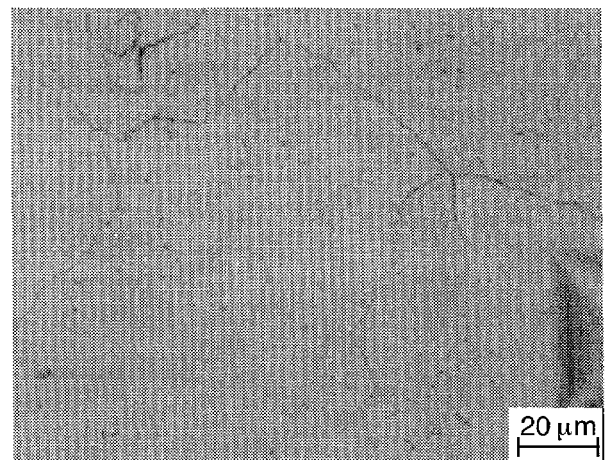
(a) Electroetched in 10% phosphoric acid solution (b) Repolished and electroetched in 5% nital solution

Figure 11. Microstructures of Alloy 690, Heat NX8625HG–21, that show continuous intergranular and some intragranular carbides
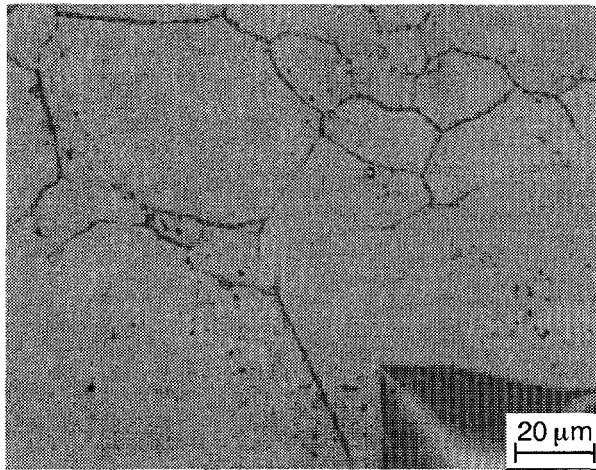
(a) Electroetched in 10% phosphoric acid solution
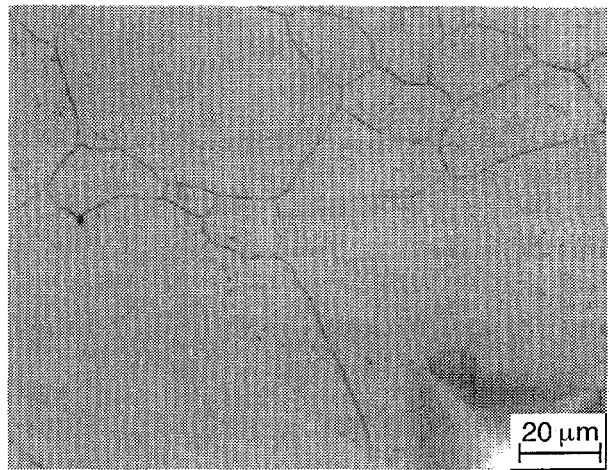
(b) Repolished and electroetched in 5% nital solution

Figure 12. Microstructures of Alloy 690, Heat NX8244HK–1A, that show continuous intergranular but few intragranular carbides
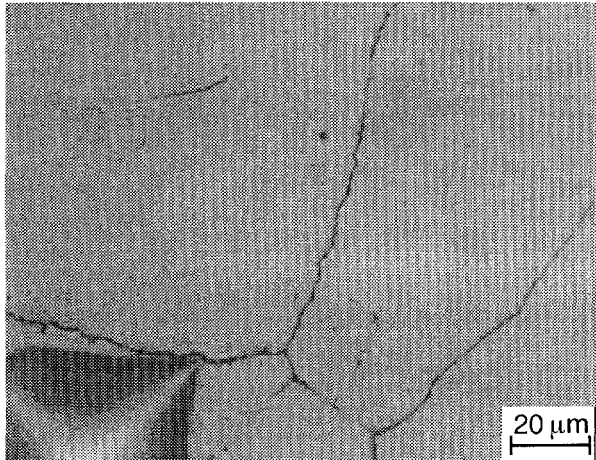
(a) Electroetched in 10% phosphoric acid solution
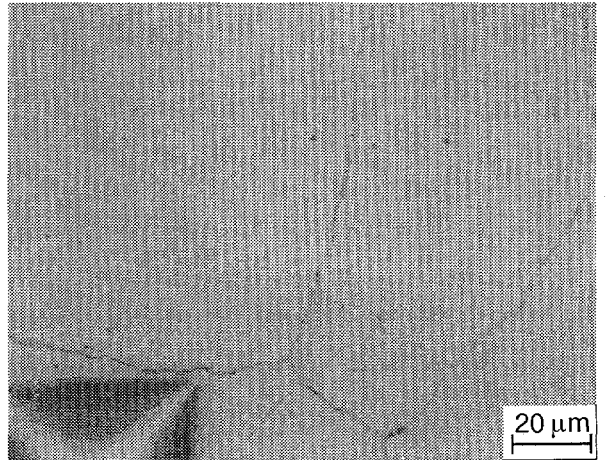
(b) Repolished and electroetched in 5% nital solution

Figure 13. Microstructures of Alloy 690, Heat NX8844HK–1B, that show continuous intergranular but few intragranular carbides
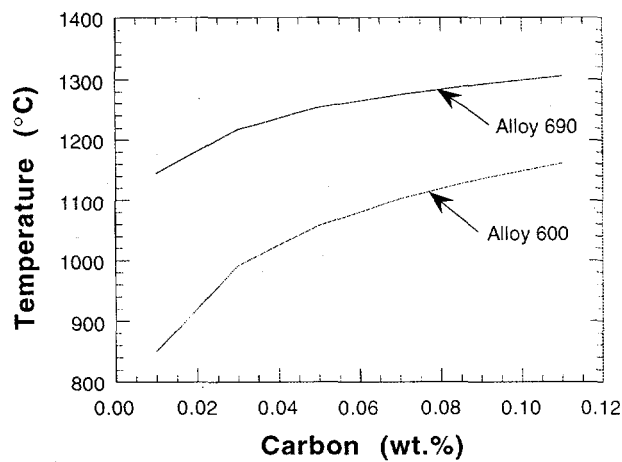
Figure 14.
Solubility of carbon in Alloys 690 and 600 vs. temperature, from Ref. 4

11

3 Fracture–Mechanics Crack Growth Tests on Alloys 600 and 690 in Simulated LWR Environments

Crack growth experiments were performed on several sets of 1TCT specimens of Alloys 600 and 690 to explore the effects of temperature, load ratio, stress intensity, and water chemistry; namely dissolved–oxygen (DO) and –hydrogen concentrations, ionic impurities (e.g., chromate and sulfate), and two organic amines on CGRs. In this investigation, the orientation of the crack plane in the specimens corresponds to L–T identification code for plates in ASTM Specification E 399. In initial experiments, CGRs of mill–annealed Alloy 600 were compared with those of sensitized Type 304 SS. Subsequently, experiments were performed on Alloy 600 and 690 specimens in high–purity (HP) water that contained a wide range of DO ($\approx$0.001–8 ppm) and hydrogen ($\approx$0–58 cm^3 $H_2 \cdot kg^{-1}$ H_2O). Experiments were also performed in simulated PWR primary–system water that contained 450 ppm boron and 2.25 ppm lithium (added to the feedwater as H_3BO_3 and LiOH), 3–58 cm^3 $H_2 \cdot kg^{-1}$ H_2O, $\approx$1 ppb DO, and 750 ppb hydrazine. Hydrazine was added to feedwater to scavenge residual DO to a very low level; however, it raised conductivity from $\approx$25 to 42 $\mu S \cdot cm^{-1}$. In these experiments, the role of H_3BO_3, LiOH, and dissolved hydrogen in crack growth was investigated vis–a–vis HP deoxygenated water. Temperature and dissolved–hydrogen concentration in water influence the stability of NiO on nickel–base alloys and conceivably could influence EAC of the alloys if a slip–dissolution or slip–oxidation mechanism for crack propagation was operative. CGRs of Alloys 600 and 690 were compared with values for wrought SSs in air, predicted by the ASME Code Section XI correlation at the K_{max} and load ratio values for the specimens in the various tests and by an Argonne Natioinal Laboratory (ANL) model for crack growth in water[5] that was modified (see Section 3.5) to account for aqueous environments that contain <0.2 ppm DO. On the basis of these scoping experiments, experimental conditions will be refined to further explore the effects of alloy heat treatment, temperature, water chemistry, and loading conditions on the EAC of the materials.

3.1 Comparison of CGRs of Sensitized Type 304 SS and Mill–Annealed Alloy 600 in Oxygenated Water

A fracture-mechanics CGR experiment was conducted on mill–annealed Alloy 600 and two sensitized Type 304 SS specimens in simulated BWR water that contained 0.2 ppm DO at conductivities in the range of $\approx$0.08 to 8.3 $\mu S \cdot cm^{-1}$. Thirteen tests were performed on a set of three specimens during an $\approx$7900 h period to compare CGR behavior of mill–annealed Alloy 600 (Heat No. J422) with that of sensitized Type 304 SS (electrochemical potentiokinetic reactivation [EPR] values of 6 and 17 Coulombs·cm^{-2}) in HP water and in water that contained sulfate and chromate impurities at low concentrations at 289°C.[6] The effect of two amines (2–butanone–oxime and ethanolamine) at low concentrations (1–5 ppm) on the CGR of the materials in oxygenated water was also investigated. The test conditions and experimental results are shown in Table 6. Most of the results were obtained at a load ratio R of 0.95 and a range of K_{max} values between 28 and 41 MPa·$m^{1/2}$. Load ratios of 0.6 and 0.8 were used in two of the tests. The frequency and rise time of the positive sawtooth wave form were 0.077 Hz and 12 s, respectively.

Experimental CGR data ($\dot{a}$) for the three specimens are plotted in Fig. 15 vs. CGRs for wrought SSs in air ($\dot{a}_{air}$), predicted by the ASME Code Section XI correlation at the K_{max} and

Table 6. Crack growth results for Alloy 600 and sensitized[a] Type 304 SS specimens under high–R loading[b] in HP oxygenated water and in oxygenated water that contained chromate, sulfate, 2–butanone–oxime, or ethanolamine at 289°C

Test No.	Test Time, h	Water Chemistry[c]					Electrode Potential			Material (Sensitization, EPR)								
		Chromate Conc.,[d] ppb	Sulfate Conc.,[d] ppb	Other Conc., ppm	Cond. at 25°C, μS·c m^-1	pH at 25°C	304 SS mV(SHE)	Pt	Load Ratio	Alloy 600			304 SS (6 C·cm^-2)			304 SS (17 C·cm^-2)		
										K_{max}[e] MPa·m1/2	ΔK,[f] MPa·m1/2	Rate, 10^{-10} m·s^{-1}	K_{max}[e] MPa·m1/2	ΔK,[f] MPa·m1/2	Rate, 10^{-10} m·s^{-1}	K_{max}[e] MPa·m1/2	ΔK,[f] MPa·m1/2	Rate, 10^{-10} m·s^{-1}
1	530–1190	–	–	–	0.09	6.24	60	98	0.95	28.0	1.40	0.10	30.4	1.52	3.1	30.7	1.54	3.7
2	1190–1232	–	–	–	0.08	6.31	65	99	0.80	28.1	5.62	0.70	30.7	6.14	6.7	31.1	6.22	6.2
3	1318–1344	–	–	–	0.08	6.31	58	84	0.60	28.4	11.36	27.0	31.2	12.48	19.0	31.4	12.56	11.0
4	1390–1910	50	–	–	0.25	6.07	61	59	0.95	28.5	1.43	0.17	31.4	1.57	2.2	31.8	1.59	2.3
5	1918–2380	200	–	–	0.74	5.64	64	32	0.95	28.7	1.44	0.078	32.4	1.62	1.4	32.8	1.64	1.9
6	2385–3162	50	15	–	0.42	6.03	71	13	0.95	29.5	1.48	3.4	33.4	1.67	1.1	33.8	1.69	1.9
7	3170–3832	50	25	–	0.47	5.93	76	37	0.95	30.6	1.53	3.3	34.2	1.71	1.4	34.3	1.72	1.2
8	3865–4323	50	100	–	1.05	5.63	94	1	0.95	31.3	1.57	2.0	35.1	1.76	3.7	35.1	1.76	2.9
9	4395–5175	50	–	–	0.27	6.11	53	–23	0.95	32.0	1.60	1.5	35.5	1.78	0.28	35.3	1.77	0.14
10	5770–6475	–	–	1.0 g	0.08	6.23	139	166	0.95	33.8	1.69	1.4	37.5	1.88	2.8	36.9	1.85	2.0
11	6490–7050	–	–	5.0 g	0.08	6.41	163	235	0.95	34.6	1.73	1.8	39.5	1.98	4.6	38.8	1.94	4.5
12	7075–7675	–	–	–	0.08	6.27	105	160	0.95	34.8	1.74	0.90	40.1	2.00	1.1	38.8	1.94	≈0
13	7770–7910	–	–	5.0 h	8.3	9.60	–3	–221	0.95	35.5	1.78	3.0	41.4	2.07	7.5	39.1	1.96	3.9

a Compact–tension specimens (1TCT) of Alloy 600 (Heat No. J422) and Type 304 SS (Heat No. 10285). The Alloy 600 specimen (No. IN–1) was tested in the as-received mill-annealed condition. The Type 304 SS specimens (Heat No. 10285) received a solution-anneal heat treatment at 1050°C for 0.5 h. Specimen No. C34 was sensitized at 650°C for 2 h (EPR = 6 C·cm^{-2}) and Specimen No. C35 at 650°C for 8 h (EPR = 17 C·cm^{-2}).

b Frequency and rise time of the positive sawtooth waveform were 8 x 10^{-2} Hz and 12 s, respectively.

c Effluent DO concentration was ≈200–300 ppb; feedwater oxygen concentration was higher by a factor of 3 to compensate for oxygen depletion by corrosion of the autoclave system.

d Chromate and sulfate were added to the feedwater as acids; average effluent chromate concentrations were ≈23 and 59 ppb for feedwater levels of 50 and 200 ppb on the basis of colorimetric analyses of grab samples.

e Stress intensity K_{max} values at the end of the time period.

f ΔK = $K_{max}(1-R)$, where load ratio R = K_{min}/K_{max}.

g 2–butanone–oxime was added to the oxygenated feedwater.

h Ethanolamine was added to the oxygenated feedwater.
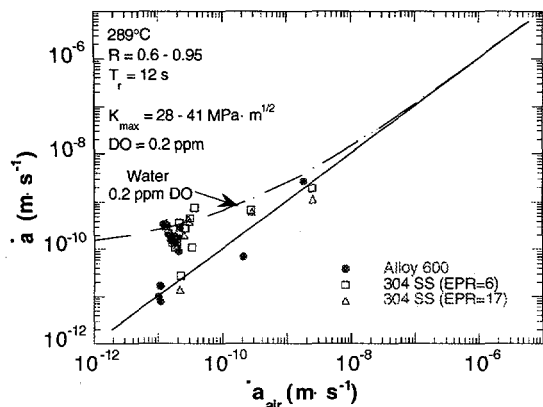
Figure 15.
Corrosion fatigue data for specimens of Alloy 600 and sensitized Type 304 SS in oxygenated water at 289°C. Dashed line represents predictions of ANL model for austenitic SSs in water with 0.2 ppm DO. Diagonal line corresponds to crack growth of SSs in air, as predicted in ASME Code.

load ratio values for the specimens in the various tests. Data for all of the materials are bounded by the two curves.

The dependence of CGRs of Alloy 600 on K_{max} at a load ratio R of 0.95 is shown in Figs. 16 together with predictions for austenitic SSs in water from the ANL model and the ASME Code in air. Several data points lie near the air line predicted by the ASME Code, i.e., the rates are not environmentally enhanced. The results suggest a threshold K_{max} for EAC of ≈26 MPa·m$^{1/2}$ at an R of 0.95, i.e., CGRs at higher K_{max} lie significantly above the air line.

To illustrate the relative effect of simulated BWR water (≈0.2 ppm DO) on EAC of Alloy 600 and sensitized Type 304 SS, the CGRs of Alloy 600 are plotted vs. the rates for the SS specimens under the same environmental and loading conditions in each test (Fig. 17). A data set in which the CGR of any of the three specimens was near the air line in Figs. 15 and 16 was omitted from the plot. A valid comparison of environmental effects on CGRs of the two materials can be made only when the specimens exhibit some degree of enhancement in the rates. Furthermore, CGRs of ≤3 x 10^{-11} m·s^{-1} (near the air line in Figs. 15 and 16) are based on small changes in crack length that are near the sensitivity of the DC potential–drop crack–length monitoring system, namely, 5 x 10^{-5} m, divided by the test times of ≈500–800 h. This can lead to a large uncertainty when comparing rates in this range. The results in Fig. 17 indicate that the CGR of mill–annealed Alloy 600 and sensitized Type 304 SS is virtually the same in simulated BWR water under the conditions in these tests.
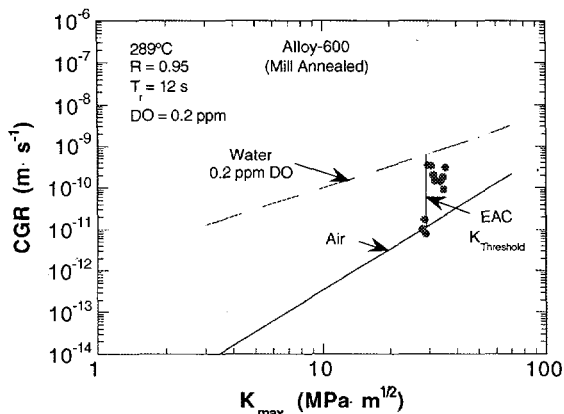
Figure 16.
Dependence of CGR of mill–annealed Alloy 600 specimen on K_{max} in oxygenated water at 289°C. Dashed and solid lines represent predictions of ANL model for austenitic SSs in water with 0.2 ppm DO and ASME Code prediction in air, respectively, at an R value of 0.95 and rise time of 12 s.
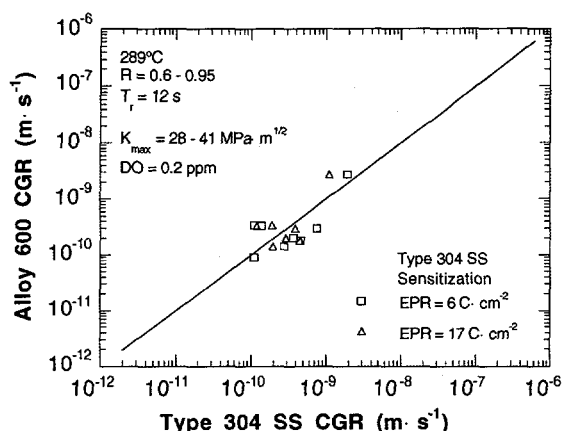
Figure 17. CGRs of Alloy 600 and two sensitized Type 304 SS specimens under identical loading and environmental conditions at 289°C. Solid line represents identical CGRs in Alloy 600 and Type 304 SS.

Plot axes: Alloy 600 CGR (m·s^{-1}) vs Type 304 SS CGR (m·s^{-1}).

289°C
R = 0.6 - 0.95
T_r = 12 s
K_{max} = 28 - 41 MPa·m$^{1/2}$
DO = 0.2 ppm

Type 304 SS Sensitization
□ EPR = 6 C·cm^{-2}
△ EPR = 17 C·cm^{-2}

The effect of water chemistry on CGRs of the materials at a load ratio of 0.95 was explored in Tests 4–13 listed in Table 6. Additions of 50 and 200 ppb chromate to feedwater produced modest decreases in the CGR of sensitized SS specimens (Tests 1, 4, and 5). At a load ratio of 0.95, CGRs of the Alloy 600 specimen were lower than those of the SS specimens by a factor of ≈10 and were not influenced by 50–200 ppb chromate in oxygenated water. In Tests 6–8, 15, 25, and 100 ppb sulfate was added to water that contained 50 ppb chromate and ≈200 ppb DO. CGRs of the sensitized Type 304 SS specimens increased by, at most, a factor of ≈3. The CGR of the Alloy 600 specimen increased from ≈8 x 10^{-12} to ≈3 x 10^{-10} m·s^{-1} when 15 ppb sulfate was added to the feedwater (Test 6), but the rate did not increase with 25 and 100 ppb sulfate. When sulfate was no longer added to oxygenated feedwater that contained 50 ppb chromate (Test 9), the CGRs of both sensitized Type 304 SS specimens decreased by a factor of 10 to ≈1–3 x 10^{-10} m·s^{-1}; the CGR of the Alloy 600 specimen remained constant at ≈1 x 10^{-10} m·s^{-1}. In the last series of experiments (Tests 10–13), chromate was not added to the feedwater and the effect of 1 and 5 ppm of 2–butanone–oxime or ethanolamine in water that contained ≈200 ppb DO was investigated. Under these water chemistry conditions, CGRs of the SS specimens increased to their previous values of ≈2–4 x 10^{-10} m·s^{-1}, and once again, the Alloy 600 specimen did not respond to changes in water chemistry. These amines at concentrations of 1–5 ppm were neither beneficial nor deleterious to CGRs of the specimens.

Thus, additions of small amounts of chromate, sulfate, and the two amines to oxygenated feedwater produced small but measurable changes in CGRs of sensitized SS specimens but had virtually no effect on CGRs of the mill–annealed Alloy 600 specimen. If the effects of these species in oxygenated water are neglected, average CGRs of the Alloy 600 and sensitized Type 304 SS (EPR = 6 and 17 C·cm^2) specimens are 2.16 x 10^{-10}, 2.65 x 10^{-10}, and 2.22 x 10^{-10} m·s^{-1}, respectively, when R = 0.95 and K_{max} >30 MPa·m$^{1/2}$. These values, i.e., ≈2 x 10^{-10} m·s^{-1}, are consistent with numerous determinations of EAC of sensitized Type 304 and nonsensitized Type 316NG SS specimens in oxygenated water at 289°C under similar loading conditions.[7] We have observed that different materials, e.g., mill–annealed Alloy 600, sensitized Type 304, nonsensitized Type 316NG, and CF–3, CF–8, and CF–8M grades of cast SSs,[8] exhibit similar CGRs in oxygenated water despite significant differences in material chemistry and microstructure. The fact that these materials exhibit different modes of crack propagation, albeit at nominally the same rate, i.e., sensitized SSs and low–carbon nuclear grade SSs exhibit intergranular and transgranular modes, respectively, whereas cracks in cast grades of austenitic SSs propagate along austenite/ferrite grain boundaries, suggests that the rate of crack propagation is controlled by the rate of cathodic reduction of DO, with a concomitant anodic dissolution process at the crack tip.

3.2 Comparison of CGRs of Mill–Annealed Alloy 600, Sensitized Type 304 SS, and Type 316NG SS in Oxygenated Water and in Simulated PWR Water

CGRs of mill–annealed Alloy 600 (Heat No. J422), Type 316NG, and sensitized Type 304 SS (EPR = 20 $C \cdot cm^{-2}$) were determined at high load ratios in simulated PWR water at 289°C. Initial tests were conducted in water that contained 450 ppm boron and 2.25 ppm lithium (added to the feedwater as H_3BO_3 and LiOH), 4.1 cm^3 $H_2 \cdot kg^{-1}$ H_2O, ≈1 ppb DO, and 750 ppb hydrazine. Room–temperature pH and conductivity were ≈7.2 and 42 $\mu S \cdot cm^{-1}$, respectively. Hydrazine was added to the feedwater to scavenge residual DO to a very low level; however, it raised conductivity from ≈25 to 42 $\mu S \cdot c \, m^{-1}$. Effluent DO and dissolved hydrogen concentrations were determined by Orbisphere oxygen and hydrogen meters. The Alloy 600 specimen was mill annealed and the Type 316NG and 304 SS specimens were solution annealed at 1050°C for 0.5 h and given sensitization heat treatments at 650°C for 24 h (EPR = 0 $C \cdot cm^{-2}$) and at 700°C for 12 h (EPR = 20 $C \cdot cm^{-2}$), respectively. CGRs were determined by the DC potential–drop method.

The usual technique to initiate fatigue cracks in specimens at 289°C in a test environment where K_{max} is 20 $MPa \cdot m^{1/2}$, load ratio is 0.2, and frequency is 10 Hz was successful for the SS specimens, but a fatigue crack did not initiate in the Alloy 600 specimen. In an attempt to initiate a crack in the latter specimen, the K_{max} and load ratio were increased to 30 $MPa \cdot m^{1/2}$ and 0.8, respectively. Under these conditions, CGRs of the Type 316NG and 304 SS specimens were ≈3.0 x 10^{-10} and 2.3 x 10^{-9} $m \cdot s^{-1}$, respectively, but once again, no crack growth occurred in the Alloy 600 specimen (Test 1 in Table 7). Because of the high CGRs of the SS specimens, the load ratio was increased from 0.8 to 0.9 in the next test. Under this condition, crack growth occurred in the Alloy 600 specimen, but the DC potential–drop measurements indicated small negative CGRs for both SS specimens. Although we could not identify the origin of the problem, we have never encountered this behavior in tests in simulated BWR water. Consequently, the water chemistry was changed from simulated primary PWR water to HP water that contained ≈6 ppm DO for a series of tests at load ratios between 0.2 and 1.0 (Tests 3–8 in Table 7). In this environment, CGRs were determined for the three specimens. Then, another attempt was made to determine CGRs in simulated PWR water by the DC potential–drop method in Tests 9 and 10. Once again, data for one of the SS specimens became erratic but results for the other and the Alloy 600 specimen exhibited normal variability. In the last test (No. 10), the hydrogen concentration was increased from ≈4 to 45 $cm^3 \cdot kg^{-1}$ to determine its effect on the CGR of the Alloy 600 specimen at a load ratio of 0.8 and a K_{max} of ≈31 $MPa \cdot m^{1/2}$. This hydrogen concentration decreased the CGR of the Alloy 600 specimen by a factor of ≈40 and increased by 45% the CGR of the Type 316NG SS specimen. The experiment was terminated and the system was reconfigured to utilize the crack–opening–displacement (COD) compliance technique for crack length measurements on specimens of Alloys 600 and 690 in simulated PWR water with a range of hydrogen concentrations.

Experimental CGR data for the Alloy 600 and Type 304 and 316NG SS specimens in HP water that contained ≈6 ppm DO are plotted in Fig. 18 vs. CGRs predicted for wrought SSs in air by the ASME Code Section XI correlation at the K_{max} and load ratio values for the specimens in the various tests. With the exception of one data point for Alloy 600, the results are bounded by the two curves.

Table 7. Crack growth results for Alloy 600, Type 316NG, and sensitized[a] Type 304 SS specimens in simulated PWR and HP oxygenated water at 289°C

Test No.	Test Time, h	Water Chemistry B[b] Conc., ppm	Li[b] Conc., ppm	H₂[c] Conc., cc·kg⁻¹	O₂[c] Conc., ppm	Cond. at 25°C, μS·cm⁻¹	pH at 25°C	Electrode Potential mV(SHE) 304 SS	Alloy 600	Load Ratio[d]	Alloy 600 K$_{max}$[e], MPa·m¹ᐟ²	ΔK[f] MPa·m¹ᐟ²	Rate, 10⁻¹⁰ m·s⁻¹	316NG SS K$_{max}$[e], MPa·m¹ᐟ²	ΔK[f] MPa·m¹ᐟ²	Rate, 10⁻¹⁰ m·s⁻¹	Material Sensitization 304 SS (20 C·cm⁻²) K$_{max}$[e], MPa·m¹ᐟ²	ΔK[f] MPa·m¹ᐟ²	Rate, 10⁻¹⁰ m·s⁻¹
1	74–113	450	2.25	4.1	0.001g	41.7	7.23	–666	–668	0.8	29.4	5.88	–h	30.3	6.06	2.97	31.0	6.20	22.9
2	118–230	450	2.25	4.1	0.001g	41.7	7.27	–731	–693	0.9	29.4	2.94	0.96	30.3	3.03	–h	31.0	3.10	–h
3	304–327	0	0	0	6.0	0.07	6.09	122	45	0.8	31.7	6.34	2.67	30.4	6.08	15.8	32.3	6.46	43.5
4	335–397	0	0	0	6.0	0.07	6.09	122	45	1.0	5.8	0	–h	5.6	0	0.27	6.0	0	2.95
5	409–422	0	0	0	5.8	0.07	6.09	128	48	1.0	15.8	0	0.48	15.5	0	0.72	16.5	0	2.13
6	471–481	0	0	0	5.8	0.07	6.09	142	53	0.5	31.7	15.85	2.37	32.0	16.00	189.0	33.6	16.80	95.0
7	495–501	0	0	0	5.8	0.07	6.09	142	53	0.2	33.1	26.48	98.0	39.2	31.36	399.0	40.5	32.40	361.0
8	504–545	0	0	0	5.2	0.07	6.09	142	55	0.8	32.7	6.54	5.72	38.9	7.78	13.4	40.3	8.06	22.8
9	640–688	450	2.25	4.0	0.001g	38.5	7.55	–748	–766	0.8	30.7	6.14	16.0	39.7	7.94	31.0	–	–	–i
10	718–788	450	2.25	45.3	0.001g	41.6	7.31	–783	–315	0.8	30.7	6.14	0.36	42.5	8.50	45.0	–	–	–i

a Compact tension specimens (1TCT) of Alloy 600 (Heat No. J422), Type 316NG (Heat No. 13198), and Type 304 SS (Heat No. 30956). The Alloy 600 specimen (No. IN–2) was tested in the as–received mill–annealed condition. Type 316NG and 304 SS specimens (Nos. 198–2 and 37, respectively) received a solution–anneal heat treatment at 1050°C for 0.5 h and were given sensitization heat treatments at 650°C for 24h (EPR = ~0 C·cm⁻², No. 198–2) and at 700°C for 12h (EPR = 20 C·cm⁻², No. 37).
b Boron and lithium were added to the feedwater as H₃BO₃ and LiOH.
c Effluent dissolved hydrogen and DO concentrations were determined with Orbisphere hydrogen and oxygen meters.
d Frequency and rise time of the positive sawtooth waveform were 8 x 10⁻² Hz and 12 s, respectively, at load ratio values of <1.0.
e Stress intensity K$_{max}$ values at the end of the time period.
f ΔK = K$_{max}$(1–R), where load ratio R = K$_{min}$/K$_{max}$.
g Effluent DO concentration was ≈1 ppb; ≈750 ppb hydrazine was added to deoxygenated feedwater to scavenge residual DO.
h Crack length measured by the DC potential–drop method indicated small negative CGRs.
i The DC potential–drop method indicated erratic large negative CGRs.
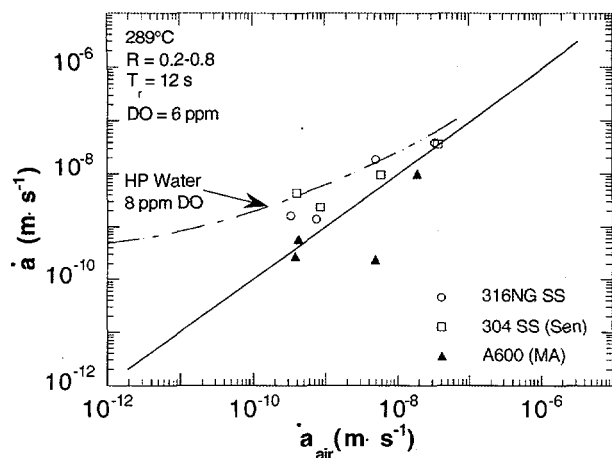
Figure 18.
Corrosion fatigue data for specimens of Alloy 600, Type 316NG and sensitized Type 304 SS in oxygenated water at 289°C. Dashed line represents predictions of ANL model for austenitic SSs in water containing 8 ppm DO. Diagonal line corresponds to crack growth of SSs in air.

Figure 19 shows experimental CGR data for the Alloy 600 and Type 304 and 316NG SS specimens in simulated PWR primary–system water that contained ≈1 ppb DO versus CGRs predicted for wrought SSs in air by the ASME Section XI correlation at the K_{max} and load ratio values for the specimens in the various tests. The dashed line represents the ANL model prediction for crack growth in water that contains ≈1 ppb DO and no contribution from stress corrosion cracking in the low–oxygen environment. With the exception of one data point for the Alloy 600 specimen, the experimental results are bounded by the predictions of the ANL model and the air line for austenitic SSs predicted by the ASME Code. Additional CGR data for austenitic SS specimens are required to validate model predictions in water that contains low DO concentrations.
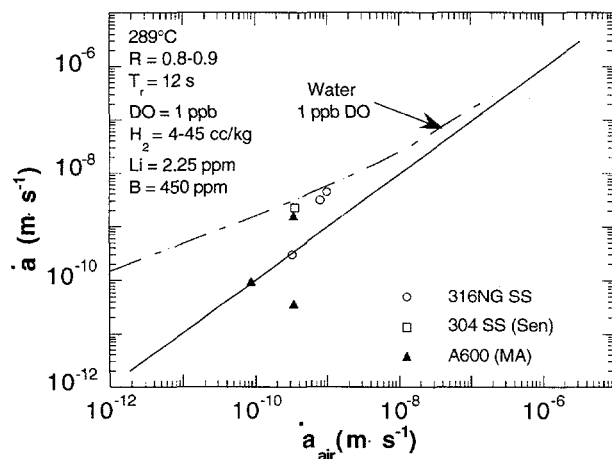
Figure 19.
Corrosion fatigue data for specimens of Alloy 600, Type 316NG and sensitized Type 304 SS in simulated PWR primary water at 289°C. Dashed line represents predictions of ANL model for austenitic SSs in water containing 1 ppb DO. Diagonal line corresponds to crack growth of SSs in air.

3.3 CGRs of Mill–Annealed Alloy 600 and Thermally Treated Alloy 690 in HP Water at 289 and 320°C

The effects of temperature, DO in HP water, and dissolved hydrogen in low-DO water on CGRs of Alloys 600 and 690 is being investigated. In the latter environment, the concentration of dissolved hydrogen in the water can influence the nature of corrosion–product films on nickel–base alloys, and thereby play a role in the crack growth process. The manner in which temperature and dissolved hydrogen in low–DO water can affect the stability of NiO on nickel and Alloy 600 (75 wt.% nickel) is outlined below.

3.3.1 Thermodynamic Stability of NiO Corrosion Product on Nickel–Base Alloys as a Function of Hydrogen Concentration of Water and Temperature

Under conditions where chemical oxidation of nickel occurs in water (Eq. 1), atomic hydrogen forms; some is absorbed by the alloy and can contribute to EAC,[9,10] the remainder is released to the coolant.

$$Ni_{(s)} + H_2O_{(g)} = NiO_{(s)} + H_{2\,(g)}. \tag{1}$$

The free–energy change ΔG_T of the reaction is given by

$$\Delta G_T = \Delta G^{\circ}_T + RT \ln K, \tag{2}$$

where ΔG°_T is the difference in the standard free energies of formation of NiO and H_2O, R is the molar gas constant, and K is the equilibrium constant of the reaction;

$$K = \frac{a_{NiO}}{a_{Ni}} \cdot \frac{a_{H_2}}{a_{H_2O}}. \tag{3}$$

If hydrogen obeys the ideal gas law in the vapor phase, and for dilute solutions of hydrogen in water; the partial pressure of hydrogen in the vapor is given by

$$pH_2 = N \cdot x, \tag{4}$$

where N is Henry's Law constant for hydrogen dissolved in water and x is the mole fraction of hydrogen gas in water.

Because the standard free energies of formation of NiO and H_2O are similar in magnitude, the standard driving force ΔG°_T for the reaction is small ($\Delta G^{\circ}_T = 550 + 10.18\ T$ cal)[10] and a high enough concentration of hydrogen in water could prevent formation of the NiO phase. For a constant hydrogen concentration in water, the pH_2/pH_2O ratio decreases as temperature increases because (a) the temperature dependence of Henry's Law constant N and thereby pH_2 decreases with temperature, and (b) the saturation pressure of water pH_2O^{sat} increases with temperature, i.e., $pH_2O \approx pH_2O^{sat}$. The dependence on temperature of ΔG_T for the reaction in Eq. 1 for 2 and 60 cm^3 $H_2 \cdot kg^{-1}$ H_2O is shown in Fig. 20. The NiO phase is not stable at positive values of ΔG_T. Figure 21 shows the calculated range of stability of NiO as a function of temperature and hydrogen concentration in deoxygenated water in units of cm^3 $H_2 \cdot kg^{-1}$ H_2O and ppm hydrogen. These results were obtained from Fig. 20 (at $\Delta G_T = 0$) and similar curves at other hydrogen concentrations in water.

According to Figs. 20 and 21, for a given dissolved H_2 concentration in water, a higher temperature favors NiO formation (a ΔG_T of <0 in Fig. 20), mainly through the ln K term in Eq. 3), in contrast to a decrease in thermodynamic stability of oxides in air and other environments as temperature increases (less negative ΔG_T). In Eq. 3, the activity of nickel in Alloy 600 was assumed to be equal to the mole fraction of nickel in the alloy, i.e., 0.72, which has only a minor effect on the position of the lines in Figs. 20 and 21. For pure nickel, the curves in these figures would be lower by $\approx 10^{\circ}C$.

For Alloy 600 and other nickel–base alloys, the calculated stability of the NiO phase (position of the line in Fig. 21) would be influenced by incorporation of chromium into the corrosion–product film, i.e., a more negative ΔG° for a nickel–chromate film. This would tend to lower the position of the line in Fig. 25 and expand the stability regime for the corrosion–

product phase. At a fixed temperature, a higher hydrogen concentration in water would be required to prevent the formation of NiO, or alternatively, at a fixed hydrogen concentration in water, a decrease in temperature would produce the same condition. Normal uncertainties in thermodynamic properties and slow oxidation kinetics (Eq. 1) at small, negative ΔG_T values near the Ni/NiO phase boundary lead to significant uncertainty when predicting whether a corrosion–product phase will actually form on the alloy surface or within a propagating crack at a given temperature and hydrogen concentration in water. Nevertheless, experimental CGR data are being obtained to determine whether these considerations are important in EAC of Alloys 600 and 690 under PWR operating conditions.
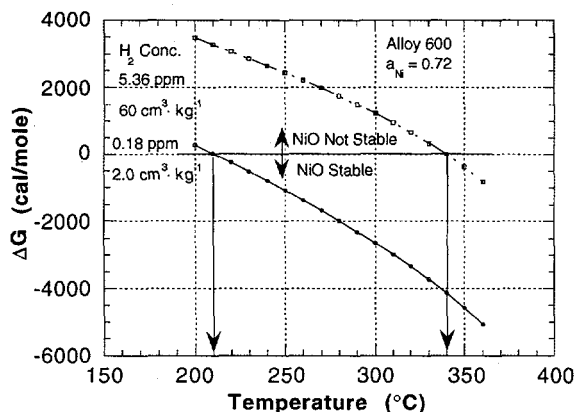
Figure 20.
Temperature dependence of free energy of formation of NiO on Alloy 600 in water containing 2 and 60 cm^3 $H_2 \cdot kg^{-1}$ H_2O. NiO is not thermodynamically stable at temperatures <210 and <340°C in water containing 2 and 60 cm^3 $H_2 \cdot kg^{-1}$ H_2O, respectively.
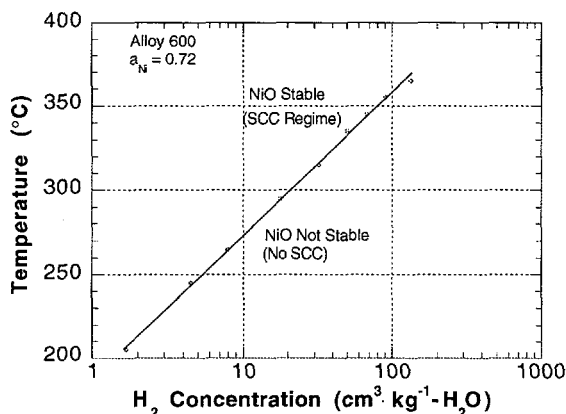
(a)
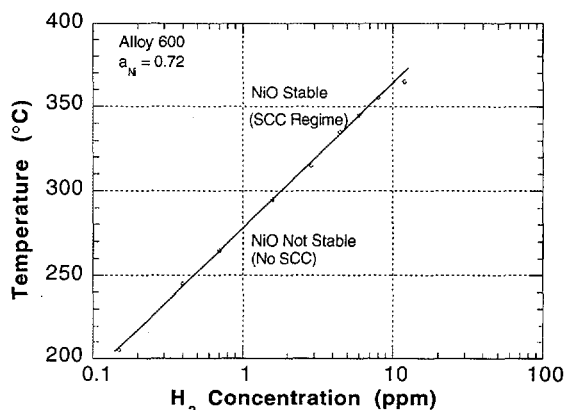
(b)

Figure 21. Calculated thermodynamic stability of NiO on Alloy 600 as a function of temperature and concentration of dissolved hydrogen in water in units of (a) cm^3 $H_2 \cdot kg^{-1}$ H_2O and (b) ppm hydrogen

3.3.2 Crack Growth Rate in HP Water

Corrosion–fatigue experiments were conducted on mill–annealed Alloy 600 (Heat No. NX8197) and mill–annealed and thermally treated Alloy 690 (NX8662HG–33) specimens in HP water to investigate the effects temperature and DO and dissolved hydrogen in water on the CGRs of these materials. The grain size (Figs. 1c and 2a) of these specimens is similar and the carbide distribution along grain boundaries of both (Figs. 7 and 10) is continuous, although Alloy 690 contains few intragranular carbides. At 290–320°C, these heats of Alloy 600 and

690 have ultimate tensile and yield strengths of $\approx$660 and 321 and 600 and 235 MPa, respectively.

Initial CGR results were obtained at 289°C in water that contained $\approx$6–8 ppm and <5 ppb DO, load ratios of 0.2, 0.6, and 0.9, and K_{max} values of 31–33 MPa·m$^{1/2}$ (Tests 1–6 in Table 8). These stress intensity factors are greater than the threshold value of $\approx$26 MPa·m$^{1/2}$ for EAC of Alloy 600 in oxygenated water (Fig. 16). Crack growth behavior of the two materials is quite similar under the conditions in these experiments. The temperature of the autoclave was increased from 289 to 320°C to begin an analogous set of experiments at the higher temperature in water that contained <5 ppb DO. During this time, the specimens were maintained at a low constant applied load before beginning the cyclic loading tests. Each incremental decrease in applied load (Tests 7–9) was accompanied by an abrupt decrease in electrical resistance of the specimens, which we attribute to closure of the tight crack, followed by a gradual increase in resistance to the inital value because of oxidation of the crack surfaces. Although the DC potential–drop measurements are indicative of crack growth at relatively low stress intensity factors, we believe that the increases in potential are caused by increases in electrical resistivity of the oxide film on crack surfaces near the crack–tip region. Eventually, the resistivities approached values obtained in the last test under cyclic loading conditions.

Two tests were conducted under cyclic loading at load ratios of 0.6 and 0.9 at a stress intensity of $\approx$33 MPa·m$^{1/2}$ (Tests 10 and 11). The CGRs at 320°C were similar to those at 289°C at the two load ratios in water with <5 ppb DO (Tests 5 and 6). Then, two tests were conducted at 320°C in water that contained $\approx$6–7 ppm DO at load ratios of 0.6 and 0.9 (Tests 12 and 13, respectively). The CGRs in these tests are similar to those at 289°C (Tests 2 and 3); i.e., CGRs of the Alloy 600 specimen show a small decrease as temperature increases at both R values. The rates for the Alloy 690 specimen at 289 and 320°C are virtually the same at a load ratio of 0.9.

Three tests were conducted at 320°C in water that contained <5 ppb DO and $\approx$0, 2.2, and 52 cm^3·kg^{-1} dissolved hydrogen at a load ratio of 0.9 (Tests 14–16, respectively), and in Test 17, the load ratio was decreased from 0.9 to 0.6 at the highest hydrogen concentration. At a load ratio of 0.9, CGRs of both specimens were low (0.5–1.3 x 10^{-11} m·s^{-1}) and dissolved hydrogen over the range of $\approx$2–53 cm^3·kg^{-1} did not have any influence on the rates at a K_{max} of $\approx$34 MPa·m$^{1/2}$. At a load ratio of 0.6, 52 cm^3·kg^{-1} hydrogen in low–DO water decreased the CGR of the Alloy 600 specimen by a factor of two at 320°C; however, the rate for the Alloy 690 specimen remained the same (compare Tests 10 and 17 in Table 8). In Tests 10 and 17, the CGRs of Alloy 690 were greater than those of Alloy 600 by factors of $\approx$2.4 and 5.4, respectively.

In Test 18 at 320°C and a load ratio of 0.6, the hydrogen concentration was decreased from $\approx$52 to 4 cm^3·kg^{-1} and the CGRs of both materials increased. In Test 19, temperature was decreased from 320 to 289°C and the load ratio was increased from 0.6 to 0.9. These changes produced a significant decrease in the CGRs of the materials. In Tests 20 and 21, load ratio was decreased from 0.9 to 0.6 and then to 0.2, respectively. The CGRs in Test 20 increased to values that were somewhat lower than those at 320°C for the same loading and water chemistry conditions (i.e., Test 18). CGRs in Tests 22 and 23 at R values of 0.9 and 0.6 in water containing $\approx$54 cm^3 H$_2$·kg^{-1} H$_2$O at 289°C were similar in magnitude to those at 320°C (Tests 16 and 17).

Table 8. Crack growth results for Alloy 600 and 690 specimens[a] in HP water at 289 and 320°C

Test No.	Test Time, h	Test Temp. °C	Water Chemistry H$_2$ Conc.,[b] cm^3·kg^{-1}	O$_2$ Conc.,[c] ppm	Cond. at 25°C, μS·cm^{-1}	pH at 25°C	Electrode Potential 304 SS mV(SHE) at 289°C	Pt	Load Ratio[d]	Alloy 600 K$_{max}$[e], MPa·m$^{1/2}$	ΔK,[f]	Rate, 10^{-10} m·s^{-1}	Alloy 690 K$_{max}$[e], MPa·m$^{1/2}$	ΔK,[f]	Rate, 10^{-10} m·s^{-1}
1	45–70	289	–	5.8	0.06	6.52	170	172	0.2	31.3	25.04	86.8	31.0	24.80	76.3
2	76–92	289	–	5.8	0.06	6.72	–	–	0.6	31.8	12.72	28.0	31.4	12.56	24.7
3	100–220	289	–	7.5	0.09	6.93	153	152	0.9	32.2	3.22	5.2	31.6	3.16	0.82
4	337–347	289	–	<0.005	0.08	6.33	–267	–400	0.2	32.5	26.00	36.7	32.2	25.76	98.3
5	348–371	289	–	<0.005	0.08	6.33	–301	–448	0.6	32.8	13.12	10.4	32.5	13.00	17.2
6	373–560	289	–	<0.005	0.06	6.83	–452	–461	0.9	32.9	3.29	0.08	32.6	3.26	0.06
7	580–720	320	–	<0.005	0.08	6.71	–488	–494	1.0	7.3	0	–g	7.3	0	–g
8	730–910	320	–	<0.005	0.08	6.81	–510	–500	1.0	5.7	0	–g	5.5	0	–g
9	915–1010	320	–	<0.005	0.09	6.81	–517	–506	1.0	1.1	0	–g	1.1	0	–g
10	1015–1035	320	–	<0.005	0.06	6.83	–522	–509	0.6	33.2	13.28	9.98	33.0	13.20	24.0
11	1035–1350	320	–	<0.005	0.08	6.55	–525	–513	0.9	33.3	3.33	0.28	33.1	3.31	0.02
12	1680–1705	320	–	5.8	0.08	6.55	168	192	0.6	33.5	13.40	22.5	33.5	13.40	38.8
13	1705–1895	320	–	7.0	0.08	6.31	249	250	0.9	33.7	3.37	1.49	33.6	3.36	0.92
14	1895–2210	320	–	<0.005	0.08	6.57	–300	–386	0.9	33.8	3.38	≈0	33.7	3.37	0.11
15	2210–2545	320	2.2	<0.001	0.09	6.40	–520	–516	0.9	33.9	3.39	0.13	33.8	3.38	0.05
16	2545–2925	320	52.1	<0.001	0.08	6.91	–610	–602	0.9	33.6	3.36	0.12	33.7	3.37	0.05
17	2925–3020	320	51.2	<0.001	0.09	6.80	–623	–614	0.6	33.9	13.56	4.28	35.1	14.04	23.0
18	4445–4470	320	3.8	<0.001	0.07	6.70	–463	–454	0.6	34.5	13.80	17.0	37.5	15.00	31.2
19	4520–4920	289	3.2	<0.001	0.06	6.78	–534	–522	0.9	34.5	3.45	0.70	37.5	3.75	≈0
20	4920–4949	289	3.8	<0.001	0.06	6.66	–544	–532	0.6	34.5	13.80	3.29	37.9	15.16	23.6
21	4968–4976	289	4.5	<0.001	0.06	6.78	–547	–535	0.2	34.8	27.84	113.70	38.6	30.88	156.6
22	5025–5385	289	53.7	<0.001	0.07	6.90	–599	–589	0.9	34.7	3.47	0.26	39.0	3.90	0.17
23	5385–5405	289	53.5	<0.001	0.07	6.90	–605	–598	0.6	34.7	13.88	0.96	39.2	15.68	16.1
24	5620–5880	289	1.8g	<0.001	0.06	6.93	–578	–563	1.0	5.7	0	2.06	6.7	0	–g
25	5940–6245	289	1.2g	<0.001	0.06	6.87	–463	–451	1.0	13.6	0	1.74	15.3	0	–g

[a] Compact tension specimens (1TCT) of Alloy 600 (Heat No. NX8197) and Alloy 690 (Heat No. NX8662HG–33). Alloy 600 and 690 specimens (Nos. 197–07 and HG–07, respectively) were tested in the as–received mill–annealed and mill–annealed plus thermally treated (715°C for 5 h) conditions, respectively.
[b] Effluent dissolved hydrogen concentration was determined with an Orbisphere hydrogen meter.
[c] Effluent DO concentration was determined with an Orbisphere oxygen meter or Chemetrics ampules.
[d] Frequency and rise time of the positive sawtooth waveform were 8 x 10^{-2} Hz and 12 s, respectively.
[e] Stress intensity K$_{max}$ values at the end of the time period.
[f] ΔK = K$_{max}$(1–R), where load ratio R = K$_{min}$/K$_{max}$.
[g] Hold periods a constant load at lower stress intensity values.
[h] Corrosion–product hydrogen; no hydrogen was added to the feedwater.

Two tests were conducted at 289°C under constant load (Tests 24 and 25) at low stress intensity factors, in which no hydrogen was added to the feedwater. The DC potential–drop response of the specimens was similar to that in Tests 7–9. When load was decreased in Test 24 and then increased in Test 25, the resistivity of both specimens first decreased and then increased abruptly, followed by a gradual increase to the values obtained at the end of Test 23. This behavior tends to confirm the hypothesis that DC potential–drop measurements are strongly influenced by morphology and degree of oxidation of crack surfaces in constant load tests if K$_{max}$ decreases, in contrast to actual increases in crack length during cyclic loading with increasing K$_{max}$.

The dependence of the CGRs of Alloy 600 and 690 specimens at 320°C on DO concentration in HP water and on the ECP of a platinum electrode (at 289°C) is shown in Fig. 22. At a load ratio of 0.6 (Figs. 22a and b), CGRs are not dependent on either DO or ECP, which is indicative of a strong contribution of cyclic loading to the rates. At a higher load ratio of 0.9, CGRs decrease as DO concentration and ECP decrease, Figs. 22c and d, respectively. Figure 23 shows similar results at 289°C at load ratios of 0.2, 0.6, and 0.9. At a high load ratio of 0.9, CGRs exhibit a 1/4–power dependence on DO concentration, which has been observed previously in slow–strain–rate tensile tests on sensitized Type 304 SSs.[11,12] The dependence of the CGRs on K_{max} at load ratios of 0.2–0.9 in deoxygenated water (<5 ppb) and in water with 6–8 ppm DO is shown in Fig. 24.
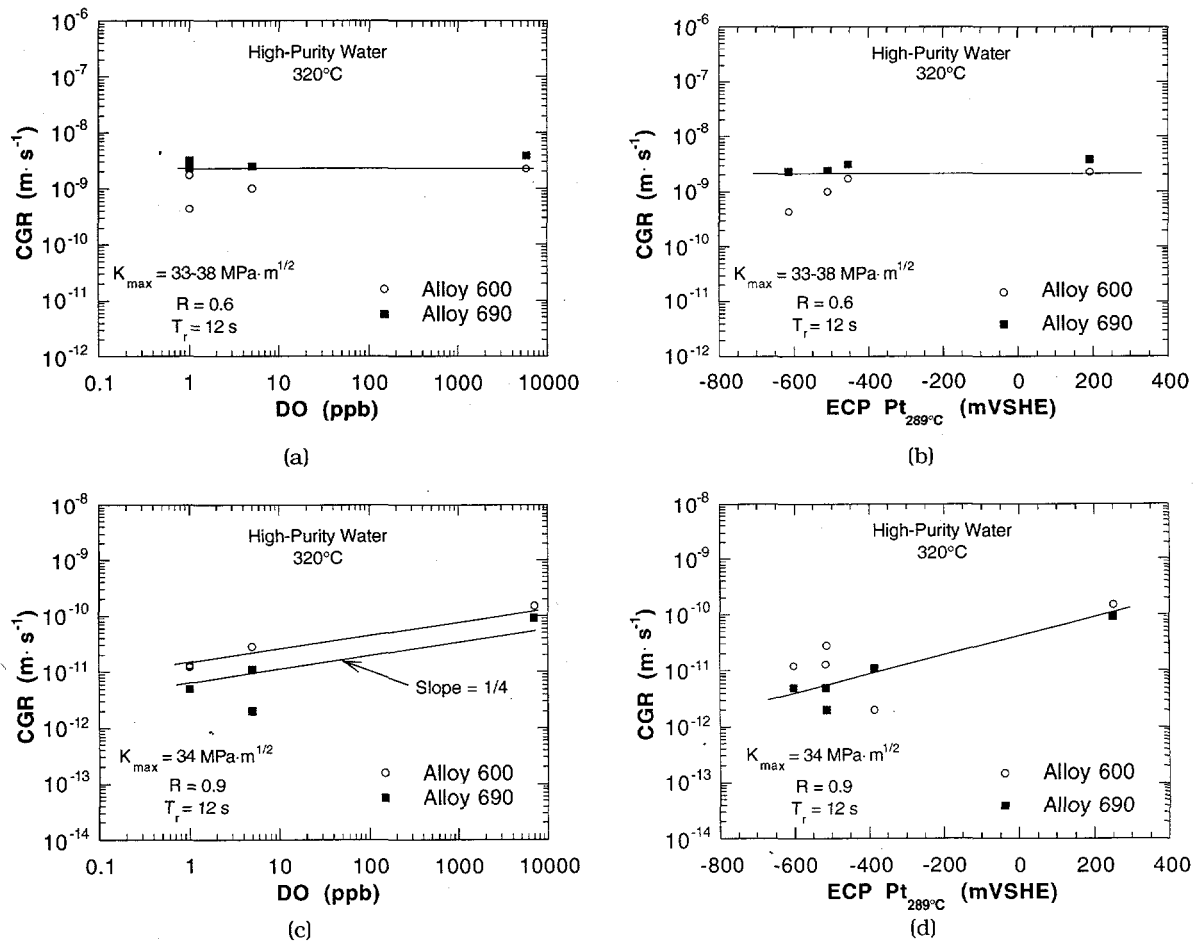
Figure 22. Dependence of CGRs of Alloy 600 and 690 specimens in HP water at 320°C on DO concentration and ECP of Pt electrode at 289°C at load ratios of 0.6 (a and b) and 0.9 (c and d), respectively

Lines that depict the predicted dependence for austenitic SSs in air from Section XI of the ASME Code at the various R values are also shown in Fig. 24. In all cases, the CGRs of both alloys lie near or below the air curve for austenitic SSs. Crack growth experiments on these alloys in air at 289 and 320°C are planned to determine whether the rates differ significantly from those of austenitic SSs and to provide baseline data for these and subsequent tests in simulated LWR environments.
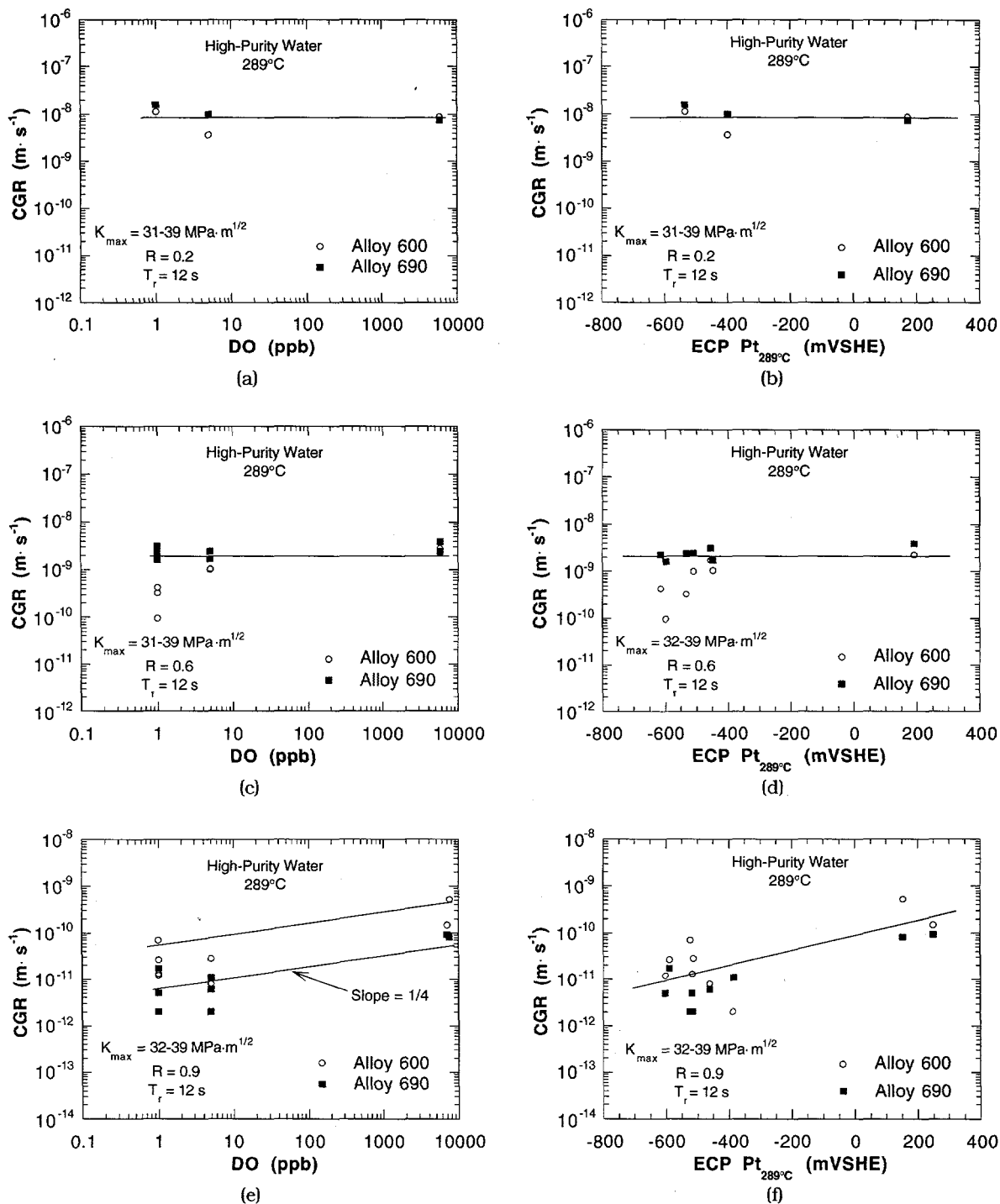
Figure 23. Dependence of CGRs of Alloy 600 and 690 specimens in HP water at 289°C on DO concentration and ECP of Pt electrode at 289°C at load ratios of 0.2 (a and b), 0.6 (c and d), and 0.9 (e and f), respectively

Corrosion–fatigue data for the alloys at 289 and 320°C are plotted vs. predicted CGRs for austenitic SSs in air from the ASME Code (Fig. 25a) and vs. rates in water predicted by the ANL model,[5] which has been modified to account for a 1/4–power dependence on DO
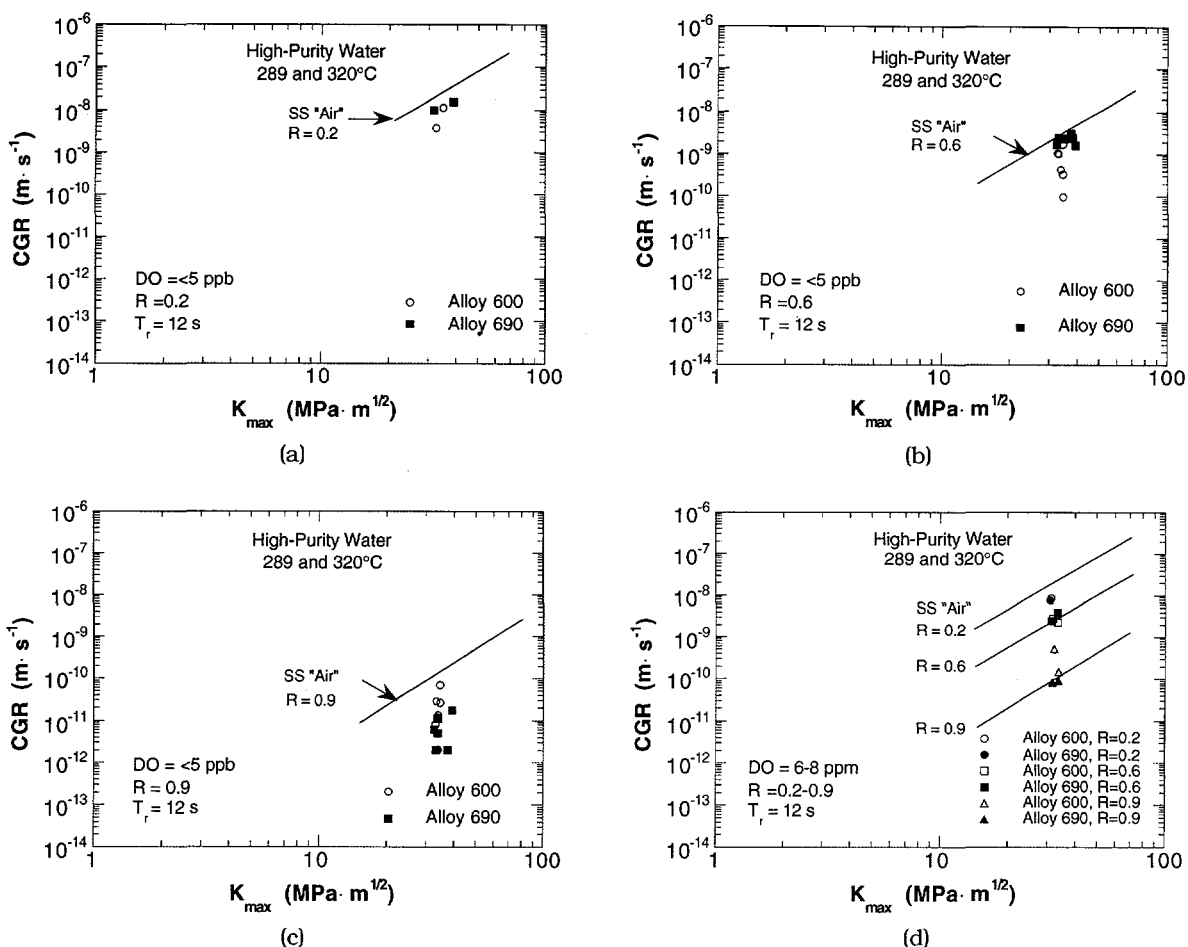
Figure 24. Dependence of CGRs of Alloy 600 and 690 specimens at 289 and 320°C on maximum stress intensity (K_{max}) in HP deoxygenated water at load ratios of (a) 0.2, (b) 0.6, and (c) 0.9, and (d) in oxygenated HP water at load ratios of 0.2, 0.6, and 0.9. Lines indicate dependence of CGRs of austenitic SSs in air on K_{max} predicted by ASME Code.

concentration in water of the environmnental contribution à $_{env}$ to crack growth (Section 3.5). Both figures indicate that the experimental data lie near or below predicted values for austenitic SSs in air or water, respectively, for the loading conditions and DO concentrations employed in these experiments. Crack growth information for nickel–base alloys in air will be sought to obtain a comparison similar to that in Fig. 25. In particular, information on CGRs of the materials in air at rates $<10^{-10}$ m·s^{-1} are required to determine whether they also deviate from the ASME–predicted air line.

3.4 CGRs of Mill–Annealed Alloy 600 and Thermally Treated Alloy 690 in Simulated PWR Water at 289 and 320°C

The influence of dissolved hydrogen in simulated PWR water on CGRs of Alloy 600 and 690 specimens from the same heats of material was determined in another series of experiments at 289 and 320°C. The water contained 450 ppm boron, 2.25 ppm lithium, <2 ppb DO, and ≈3–58 cm^3 H$_2$·kg^{-1} H$_2$O. Because of problems encountered with the DC
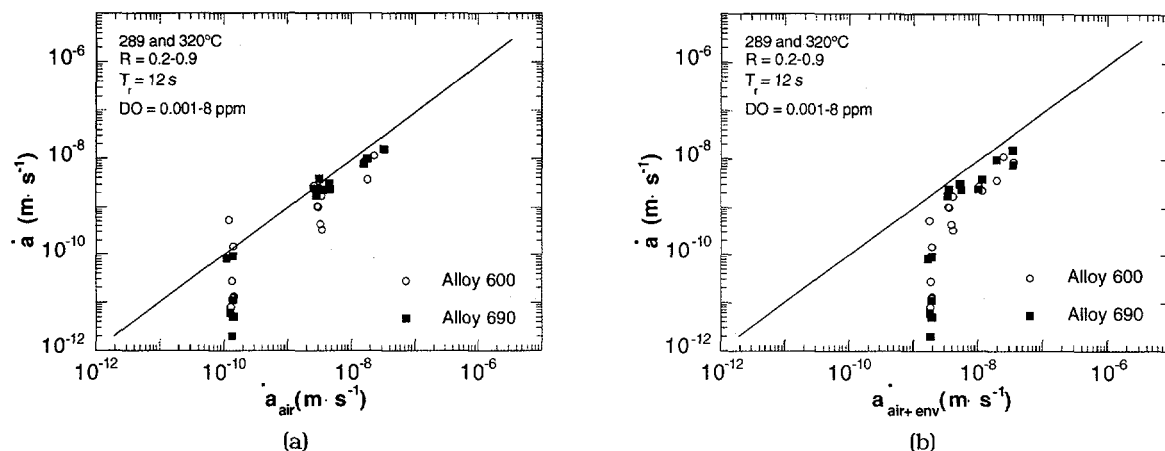
Figure 25. Corrosion fatigue data for Alloy 600 and 690 specimens in HP water at 289 and 320°C vs. (a) CGRs for SSs in air, predicted by ASME Code, and (b) CGRs for SSs in water predicted by ANL model, both under same loading conditions as in experiments. Lines represent identical CGRs for these alloys in test environments and for SSs in (a) air and (b) water.
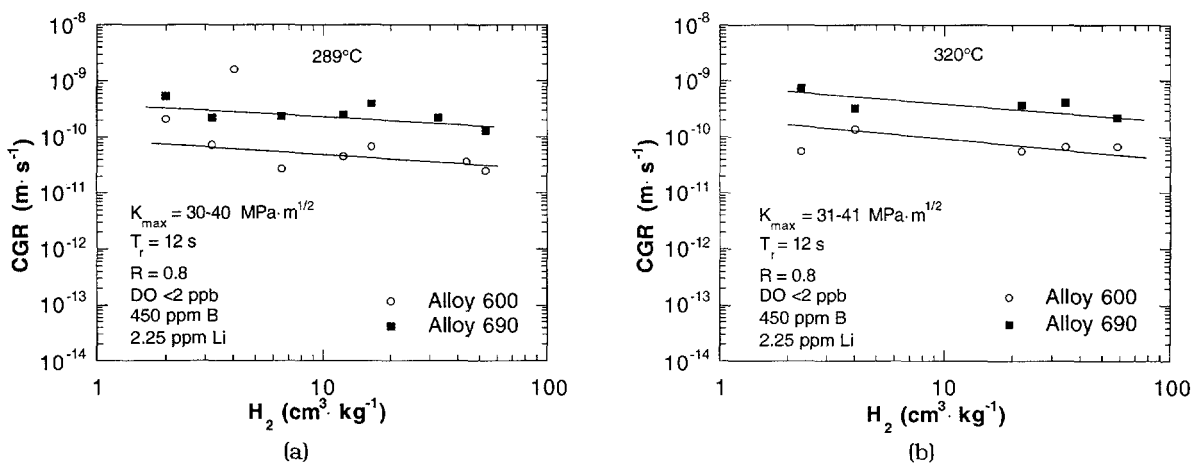
Figure 26. Dependence of CGRs of Alloy 600 and 690 specimens at (a) 289 and (b) 320°C on concentration of dissolved hydrogen in simulated PWR water at load ratio of 0.8

potential–drop technique, crack length was determined by the compliance method with the use of MTS clip gages. Tests were conducted at a load ratio of 0.8 and K_{max} in the range $\approx$30–39 MPa·m$^{1/2}$. The results are given in Table 9 and plotted in Fig. 26.

CGRs decreased slightly as dissolved hydrogen concentration increased from 3 to 58 cm^3·kg^{-1}. The Alloy 690 specimen exhibited a higher CGR by a factor of $\approx$3 than Alloy 600 under these water chemistry conditions at both temperatures. A somewhat larger decrease in the CGRs was expected, based on a predicted change in the thermodynamic stability of NiO corrosion product on the alloys as the concentration of dissolved hydrogen in the water increased or as the temperature decreased in these experiments. More experimental CGR data are required to deduce whether these considerations are important in EAC of Alloy 600 and other nickel–base alloys under PWR operating conditions.

Table 9. Crack growth results for Alloy 600 and 690 specimens[a] in simulated PWR water at 289 and 320°C

| Test No. | Test Temp, °C | Test Time, h | Water Chemistry | | | | | | Electrode Potential mV(SHE) at 289°C | | Load Ratio[e] | Alloy 600 | | | Alloy 690 | | |
			B Conc.,[b] ppm	Li Conc.,[b] ppm	H₂ Conc.,[c] cm³·kg⁻¹	O₂ Conc.,[d] ppb	Cond. at 25°C, µS·cm⁻¹	pH at 25°C	304 SS	Alloy 600		K$_{max}$[f] MPa·m$^{1/2}$	ΔK,[g] MPa·m$^{1/2}$	Rate, 10⁻¹⁰ m·s⁻¹	K$_{max}$[f] MPa·m$^{1/2}$	ΔK,[g] MPa·m$^{1/2}$	Rate, 10⁻¹⁰ m·s⁻¹
1	289	0–540	450	2.25	53.0	<2	26	7.23	–798	–805	0.8	30.3	6.06	0.25	30.7	6.14	1.29
2	320	540–1020	450	2.25	58.0	<2	31	7.32	–805	–809	0.8	30.6	6.12	0.68	31.3	6.26	2.19
3	320	1020–1550	450	2.25	4.0	<2	35	7.32	–760	–757	0.8	31.0	6.20	1.35	32.4	6.48	3.25
4	289	1550–2010	450	2.25	3.2	<2	36	7.42	–745	–741	0.8	31.2	6.24	0.73	33.0	6.60	2.20
5	289	2010–2550	450	2.25	6.5	<2	38	7.39	–755	–758	0.8	31.4	6.28	0.27	33.9	6.78	2.30
6	289	2550–2790	450	2.25	12.3	<2	41	7.27	–777	–780	0.8	31.4	6.28	0.45	34.3	6.86	2.51
7	289	2790–3270	450	2.25	16.4	<2	39	7.29	–771	–773	0.8	31.8	6.36	0.68	35.7	7.14	3.93
8	320	3275–3730	450	2.25	22.0	<2	40	7.28	–732	–737	0.8	31.9	6.38	0.56	36.9	7.38	3.73
9	320	3732–4086	450	2.25	34.4	<2	38	7.28	–785	–791	0.8	32.1	6.42	0.68	38.0	7.60	4.19
10	289	4088–4430	450	2.25	32.7	<2	38	7.27	–784	–794	0.8	32.1	6.42	≈0	38.6	7.72	2.18
11	289	4760–5070	450	2.25	2.0h	<2	37	7.26	–745	–720	0.8	32.4	6.48	2.09	39.9	7.98	5.39
12	320	5070–5310	450	2.25	2.3h	<2	36	7.26	–739	–736	0.8	32.7	6.54	0.56	41.4	8.28	7.51

a Compact tension specimens (1TCT) of Alloy 600 (Heat No. NX8197) and Alloy 690 (Heat No. NX8662HG–33). The Alloy 600 and 690 specimens (Nos. 197–09 and HG–09, respectively) were tested in the as-received mill-annealed and annealed plus thermally treated (715°C for 5 h) conditions, respectively.
b Boron and lithium were added to the feedwater as H₃BO₃ and LiOH.
c Effluent dissolved hydrogen concentration was determined with an Orbisphere hydrogen meter.
d Effluent DO concentration was <2 ppb; ≈750 ppb hydrazine was added to deoxygenated feedwater to scavenge residual DO, which was measured with Chemetrics ampules for the "ultra low range."
e Frequency and rise time of the positive sawtooth waveform were 8 x 10⁻² Hz and 12 s, respectively.
f Stress intensity K$_{max}$ values at the end of the time period.
g ΔK = K$_{max}$(1–R), where load ratio R = K$_{min}$/K$_{max}$.
h Corrosion–product hydrogen; hydrogen was not added to the feedwater.

27

3.5 Dependence on ΔK of CGRs of Mill–Annealed Alloy 600 and Thermally Treated Alloy 690 in HP and Simulated PWR Water at 289 and 320°C

Exploration of the dependence of CGRs of mill–annealed Alloy 600 and thermally treated Alloy 690 specimens at 289 and 320°C on ΔK can be based on tests performed in HP and simulated PWR water (Tables 8 and 9, respectively) at several load ratios. The results were compared with predictions of the ANL model for crack growth of austenitic SSs in water.[5] Briefly, the CGR $\dot{a}_{super}$ in an aqueous environment is written as a superposition of a term that represents the contribution of SCC under constant load $\dot{a}_{SCC}$; a corrosion–fatigue term $\dot{a}_{env}$, representing the additional CGR under cyclic loading due to the environment; and a mechanical fatigue term $\dot{a}_{air}$, representing fatigue–crack growth in air,

$$\dot{a}_{super} = \dot{a}_{SCC} + \dot{a}_{env} + \dot{a}_{air} \tag{5}$$

The SCC term was obtained from a correlation given in U.S. Nuclear Regulatory Commission (NRC) Report NUREG–0313, Rev. 2, January 1988. The correlation was based largely on data in water that contained 8 ppm DO at impurity levels typically higher than those found in currently operating plants. To account for additional data at 200 ppb DO and more representative impurity levels, the CGR is taken as one–third that given in NUREG–0313:

$$\dot{a}_{SCC} = 2.1 \times 10^{-13} \, K^{2.161} \quad (m \cdot s^{-1}) \quad 8 \text{ ppm DO} \tag{6}$$

$$\dot{a}_{SCC} = 7.0 \times 10^{-14} \, K^{2.161} \quad (m \cdot s^{-1}) \quad 200 \text{ ppb DO,}$$

where K is the stress intensity factor in $MPa \cdot m^{1/2}$. The contribution from SCC is assumed to be negligible for deoxygenated HP water and for PWR primary–water–chemistry conditions; consequently, the CGR is given by

$$\dot{a} = \dot{a}_{env} + \dot{a}_{air}. \tag{7}$$

The air term, based on the work of James and Jones,[13] is given by the current ASME Code Section XI correlation at 288°C as

$$\begin{aligned} \dot{a}_{air} &= 3.43 \times 10^{-12} \, S(R) \, \Delta K^{3.3} / T_R \\ S(R) &= 1 + 1.8 R \qquad\qquad R \le 0.8 \\ &= -43.35 + 57.97 R \qquad R > 0.8 \end{aligned} \tag{8}$$

where T_R is the rise time in s of the loading wave form, R is the load ratio (K_{min}/K_{max}), and ΔK is $K_{max} - K_{min}$. Following Shoji[14] and Gilman et al.,[15] the corrosion–fatigue term is assumed to be related to $\dot{a}_{air}$ through a power law

$$\dot{a}_{env} = A \, \dot{a}_{air}^m. \tag{9}$$

The values of the coefficient A and the exponent m for water with 200 ppb DO at 288°C were obtained by an empirical power–law–curve fit to the existing data for austenitic SSs at R <0.9, where cyclic loading dominates and the stress corrosion term in the superposition model (Eq. 5) can be ignored. The values are

$$\begin{aligned} A &= 4.5 \times 10^{-5} \\ m &= 0.5 \end{aligned} \tag{10}$$

for CGRs in $m \cdot s^{-1}$ and K in $MPa \cdot m^{1/2}$. In water that contains 8 ppm DO at 288°C, an empirical power–law–curve fit to the available data gives

$$A = 1.5 \times 10^{-4}$$

$$m = 0.5. \tag{11}$$

As was mentioned previously, the dependence of CGRs of austenitic SSs on DO concentration $[O_2]$ follows an $\approx[O_2]^{1/4}$ relationship over this range of oxygen concentrations.[11,12] The results for Alloys 600 and 690 in Figs. 22c and 23e also exhibit this dependence on DO. To compare model predictions with CGRs in water that contains low DO levels, the values of A at 200 ppb and 8 ppm were fit to a power–law relationship and the constant A in Eq. 9 is given by the relationship

$$A = 1.08 \times 10^{-5} (DO)^{0.287}. \tag{12}$$

From Eq. 8, it is evident that $\dot{a}_{air}$ exhibits a complex dependence on R; therefore, the predicted dependence of the crack growth rate $\dot{a}$ on ΔK can be obtained from Eqs. 7–9, and 12 at differing values of R. Figure 27 shows the predicted dependence of $\dot{a}$ on ΔK in 288°C water that contains 1 ppb DO at several R values between 0.2 and 0.95, a rise time of 12 s, and K_{max} between 3 and 100 MPa·m$^{1/2}$. At R values ≤ 0.8, the curves do not differ significantly, whereas, at higher R values, the range of $\dot{a}$ is wider for a given ΔK.
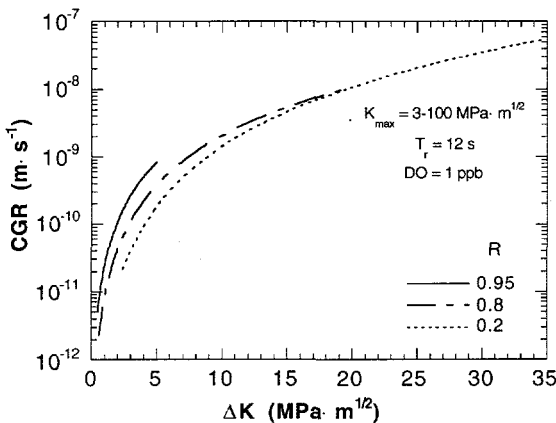
Figure 27.
Dependence of CGR at 288°C on ΔK for R of 0.2, 0.8, and 0.95 in water containing 1 ppb DO, predicted by ANL model

The relative contribution of the $\dot{a}_{air}$ and $\dot{a}_{env}$ terms in the model at several R values between 0.2 and 0.95 is shown in Fig. 28. At ΔK values $\approx$>5 MPa·m$^{1/2}$, mechanically induced crack growth, i.e., $\dot{a}_{air}$, is the major contributor to the rate, whereas, at values $\approx$<5 MPa·m$^{1/2}$, the $\dot{a}_{env}$ term is similar in magnitude to $\dot{a}_{air}$. At low ΔK, i.e., 3–5 MPa·m$^{1/2}$, $\dot{a}_{air}$ and $\dot{a}_{env}$ are $\approx$1 x 10^{-10} m·s^{-1} over the entire range of R. Thus, to explore EAC of these materials, experiments should be conducted at low ΔK and at $K_{max} > K_{Threshold}$, where significant enhancement in the rates should occur.

Experimental CGR data for Alloys 600 and 690 from Tables 8 and 9 can be compared with model predictions. Figures 29 and 30 show the dependence of CGRs of mill–annealed Alloy 600 and thermally treated Alloy 690 specimens at 289 and 320°C on ΔK at constant load ratios in deoxygenated HP and simulated PWR water, respectively. The experiments were not conducted by adjusting (increasing) ΔK at constant R values, rather, the data were obtained by adjusting R at a given K_{max}, in which K_{max} increases slowly as crack length increases during the course of the experiments. The data in both environments are consistent with the trend lines depicted in the figures; however, in some instances, experimental CGRs for Alloy 690 at high R (0.9) lie significantly below the trend lines. The current results on Alloy 690 were obtained from a heat that has a relatively low yield stress when compared with that of Alloy
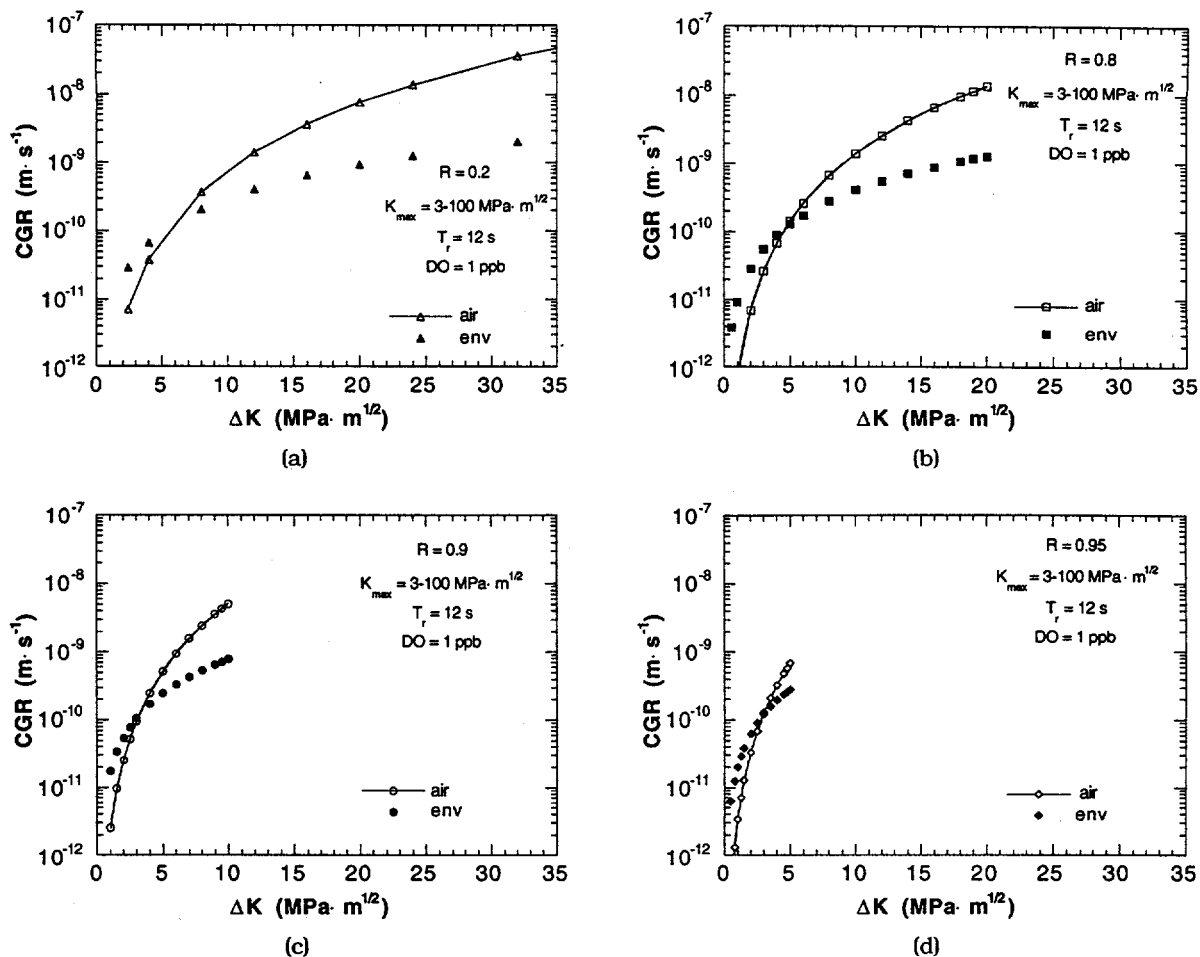
Figure 28. Contribution of air and deoxygenated–water terms in model to crack growth rate at 288°C vs. ΔK at load ratios of (a) 0.2, (b) 0.8, (c) 0.9, and (d) 0.95

600 (≈232 vs. 327 MPa at 320°C). Because mechanically driven crack growth can be correlated with yield stress, this could be simply a heat–to–heat variation. The data at several load ratios also suggest that there is a threshold ΔK at which rates increase significantly with a minimal increase in ΔK, and then increase more slowly as ΔK increases in a manner consistent with model predictions. At load ratios ≤0.8, it appears that CGRs of the Alloy 690 specimens are slightly higher than those of Alloy 600; however, at an R of 0.9 the rates for both alloys are similar. Threshold ΔKs are indicated in Figs. 27 and 28 and the values are plotted vs. load ratio in Fig. 31. The dependence of $\Delta K_{Threshold}$ on load ratio for both alloys in deoxygenated water at 289 and 320°C is given by the equation

$$\Delta K_{th} = 32.0 \ (1-R). \qquad (13)$$

Crack growth experiments will be conducted on specimens from other heats of the alloys at high load ratios, including constant load (R = 1.0), to determine the effect of yield stress on the rates, and whether Alloy 690 exhibits lower rates than Alloy 600 at higher R values.
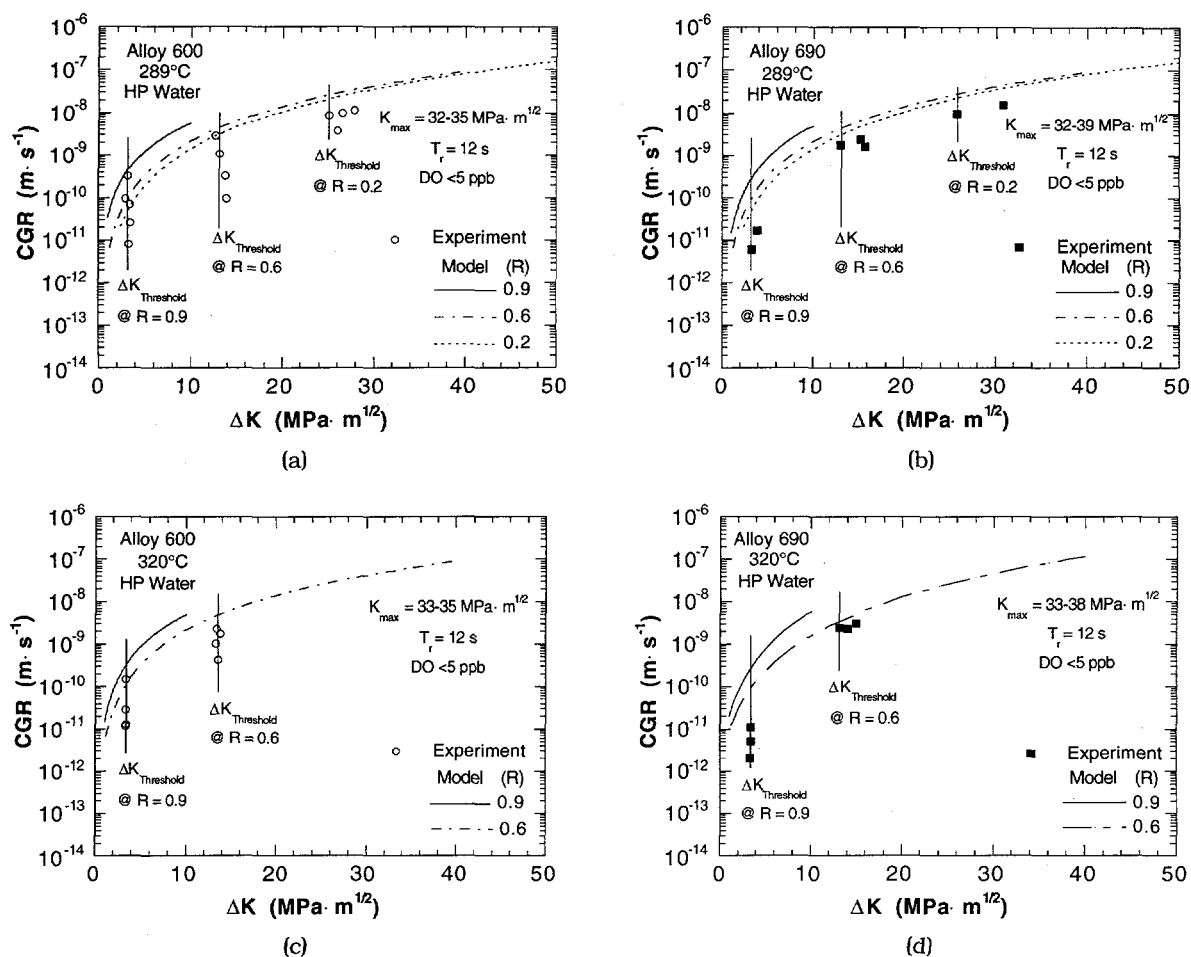
Figure 29. Dependence of CGRs of Alloy 600 and 690 specimens in deoxygenated HP water on ΔK at (a) and (b) 289, and (c) and (d) 320°C

3.6 Morphology of Crack Path and Surface of Alloy 600 and 690 Specimens

Morphology of corrosion–fatigue cracks in the Alloy 600 and 690 specimens listed in Tables 6–9 has been determined. The 1TCT specimens were sectioned vertically, and one–half of each specimen was split in the plane of the crack in liquid nitrogen. Corrosion–product films were removed from the fracture surface by a chemical process to reveal the morphology of the underlying material. The intact portion of the specimen that encompassed the crack was polished and etched to corroborate the mode of crack propagation and also to determine if crack branching had occurred during the test. The total crack lengths at the end of the test were consistent with values obtained by DC potential–drop and compliance techniques.

Figures 32–37 show the fracture surface, fracture morphology, and crack path in the crack–tip region of the specimens. The Alloy 600 specimen (Table 6), which has a very small grain size, exhibited intergranular cracking in oxygenated water (Fig. 32). The crack path in the Alloy 600 specimen in which the environment at the beginning and end of the experiment was simulated primary PWR, with an intermediate period of oxygenated HP water (Table 7), revealed transgranular cracking under all conditions (Fig. 33). The Type 316NG and
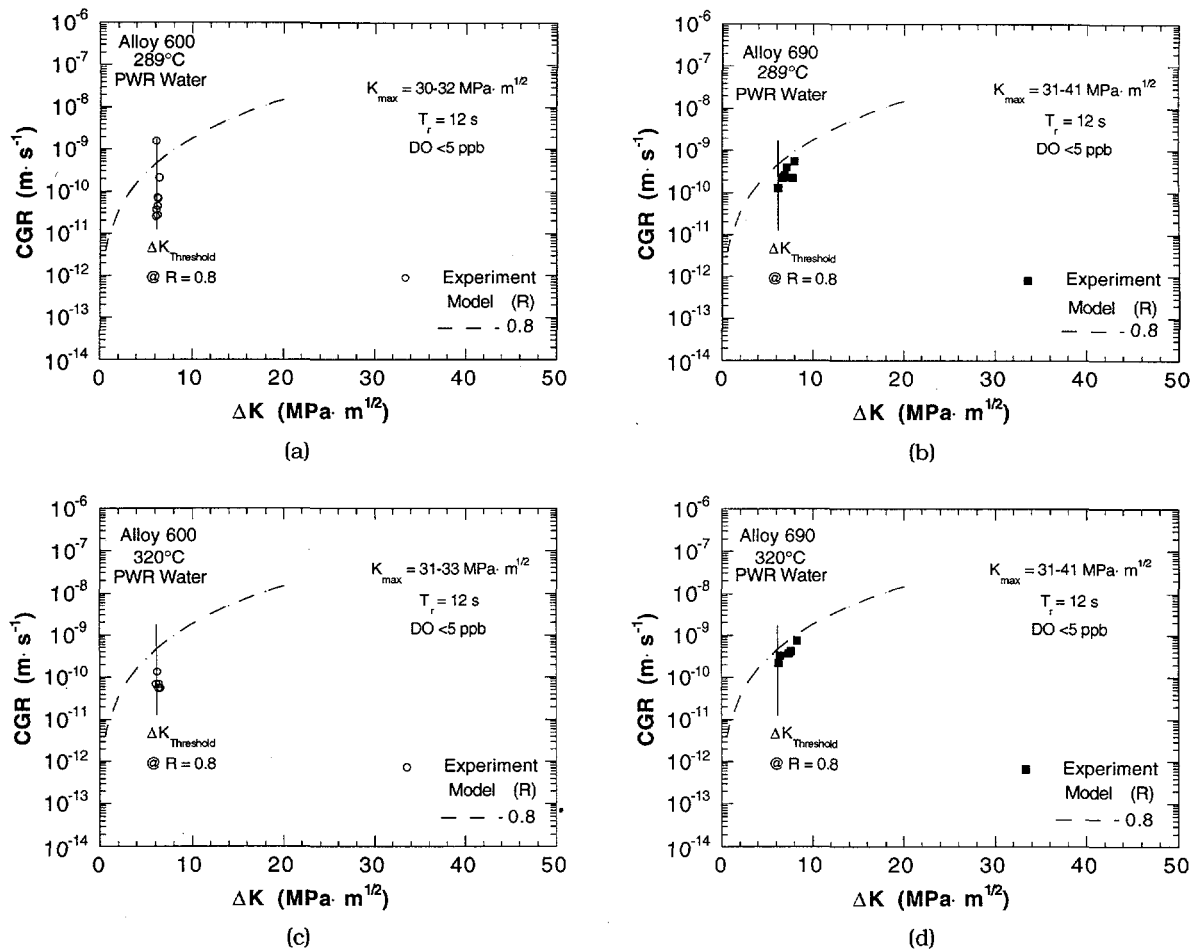
Figure 30. Dependence of CGRs of Alloy 600 and 690 specimens in simulated PWR water on ΔK at (a) and (b) 289, and (c) and (d) 320°C
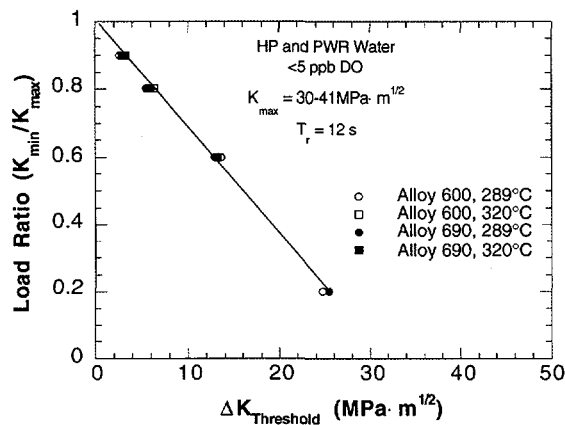
Figure 31.
Dependence of ΔK_{th} for Alloy 600 and 690 specimens in simulated PWR and de-oxygenated HP water on load ratio at 289 and 320°C

sensitized Type 304 SS specimens also exhibited a transgranular mode of crack propagation during tests in simulated PWR water and in oxygenated HP water.[6] Intergranular cracking of the sensitized Type 304 SS specimen in oxygenated water was not observed because of the low load ratio in most of the tests.

ALLOY 600	HEAT TREATMENT	LOAD CONDITIONS	ENVIRONMENT
Spec. No. IN-1 Heat No. J422	Mill annealed	K_{max} = 28–36 MPam$^{1/2}$ R = 0.60–0.95 Freq. = 0.077 Hz	200–300 ppb DO 0–200 ppb Chromate 0–100 ppb Sulfate

CRACK TIP REGION   FRACTURE SURFACE   FRACTURE MORPHOLOGY

Figure 32. Crack path, fracture surface, and fracture morphology of 1TCT specimen of Alloy 600 (No. IN–1) after crack growth experiment in oxygenated HP water and oxygenated water containing chromate, sulfate, 2–butanone–oxime, or ethanolamine at 289°C

ALLOY 600	HEAT TREATMENT	LOAD CONDITIONS	ENVIRONMENT
Spec. No. IN-2 Heat No. J422	Mill annealed	K_{max} = 29–31 MPam$^{1/2}$ R = 0.2–1.0 Freq. = 0.077 Hz at R <1.0	HP Water: 6 ppm DO and PWR: 450 ppm B, 2.25 ppm Li, 4–45 cm^3 H$_2$ kg^{-1}H$_2$O

CRACK TIP REGION   FRACTURE SURFACE   FRACTURE MORPHOLOGY

Figure 33. Crack path, fracture surface, and fracture morphology of 1TCT specimen of Alloy 600 (No. IN–2) after crack growth experiment in HP water and simulated PWR water at 289°C

ALLOY 600	HEAT TREATMENT	LOAD CONDITIONS	ENVIRONMENT
Spec. No. 197–07	Mill annealed	$K_{max} = 31\text{--}35 \text{ MPam}^{1/2}$	<0.005–7.5 ppm DO
Heat No. NX8197		$R = 0.2\text{--}1.0$	0–53 cm³ $H_2 \cdot kg^{-1}$ H_2O
		Freq. = 0.077 Hz, R <1.0	0.06–0.09S·cm⁻¹

OUTER SURFACE

B/2

DUCTILE

CF

CRACK TIP REGION   FRACTURE SURFACE   FRACTURE MORPHOLOGY

Figure 34. Crack path, fracture surface, and fracture morphology of 1TCT specimen of Alloy 600 (No. 197–07) after crack growth experiment in HP water at 289 and 320°C

ALLOY 690	HEAT TREATMENT	LOAD CONDITIONS	ENVIRONMENT
Spec. No. HG–07	Mill annealed plus 715°C for 5 h	$K_{max} = 31\text{--}39 \text{ MPam}^{1/2}$	<0.005–7.5 ppm DO
Heat No. NX8662HG–33		$R = 0.2\text{--}1.0$	0–53 cm³ $H_2 \cdot kg^{-1} H_2O$
		Freq. = 0.077 Hz, R <1.0	0.06–0.09S·cm⁻¹

OUTER SURFACE

B/2

DUCTILE

CF

CRACK TIP REGION   FRACTURE SURFACE   FRACTURE MORPHOLOGY

Figure 35. Crack path, fracture surface, and fracture morphology of 1TCT specimen of Alloy 690 (No. HG–07) after crack growth experiment in HP water at 289 and 320°C

ALLOY 600	HEAT TREATMENT	LOAD CONDITIONS	ENVIRONMENT
Spec. No. 197–09	Mill annealed	$K_{max} = 30\text{--}33 \text{ MPam}^{1/2}$	PWR; <2 ppb DO
Heat No. NX8197		$R = 0.8$	2–58 cm³ $H_2 \cdot kg^{-1}$ H_2O
		Freq. = 0.077 Hz	450 ppm B, 2.25 ppm Li

OUTER SURFACE

B/2

DUCTILE

CF

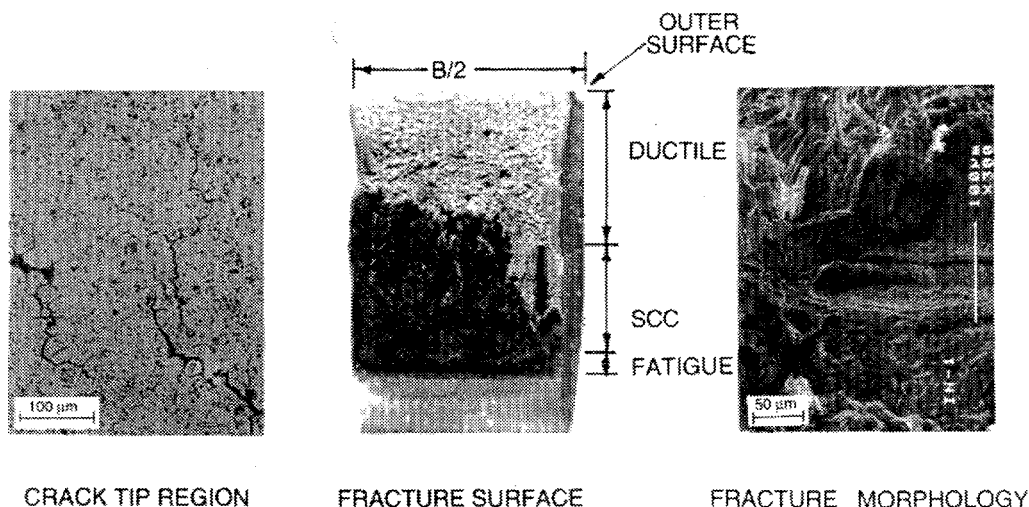CRACK TIP REGION   FRACTURE SURFACE   FRACTURE MORPHOLOGY

Figure 36. Crack path, fracture surface, and fracture morphology of 1TCT specimen of Alloy 600 (No. 197–09) after crack growth experiment in simulated PWR water at 289 and 320°C

ALLOY 690 Spec. No. HG–09 Heat No. NX8662HG–33	HEAT TREATMENT Mill annealed plus 715°C for 5 h	LOAD CONDITIONS K_{max} = 31–41 $MPa·m^{1/2}$ R = 0.80 Freq. = 0.077 Hz	ENVIRONMENT PWR; <2 ppb DO 2–58 cm^3 H_2 kg^{-1} H_2O 450 ppm B, 2.25 ppm Li

CRACK TIP REGION   FRACTURE SURFACE   FRACTURE MORPHOLOGY

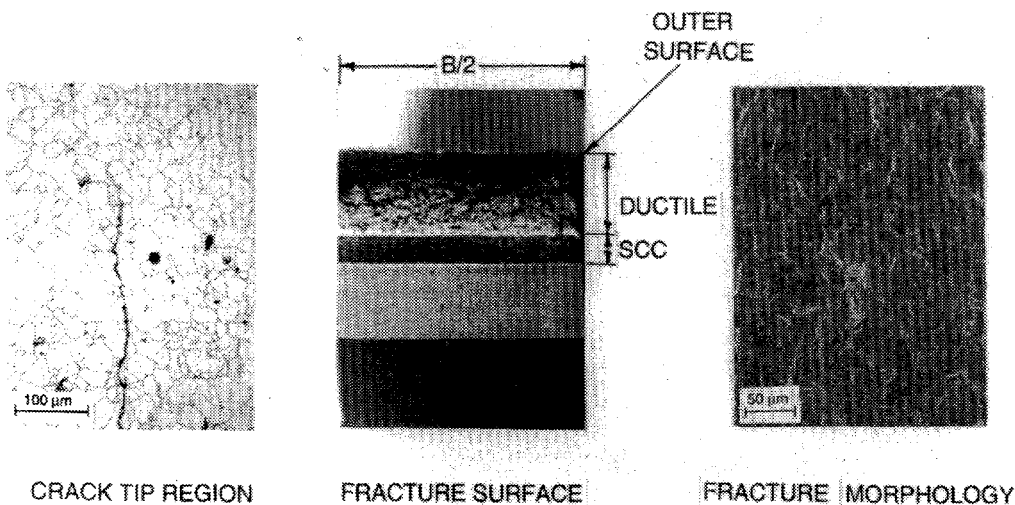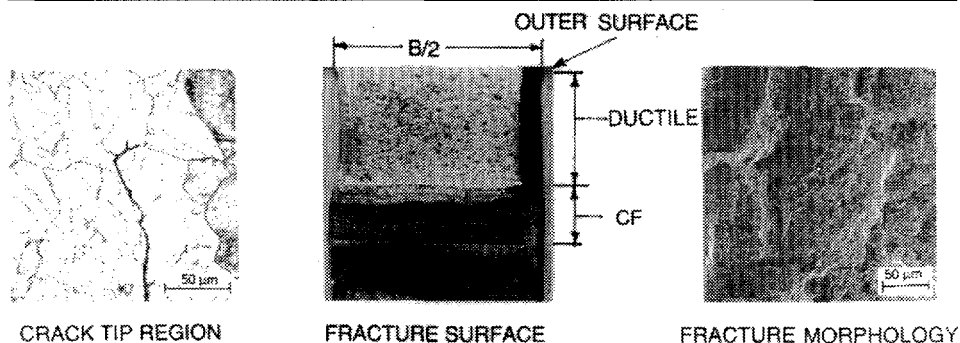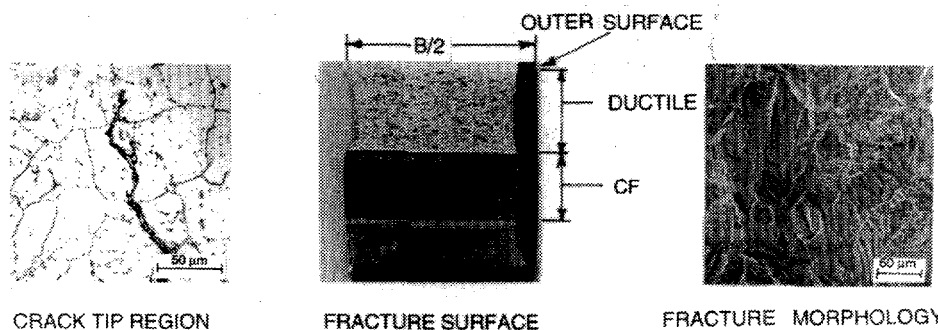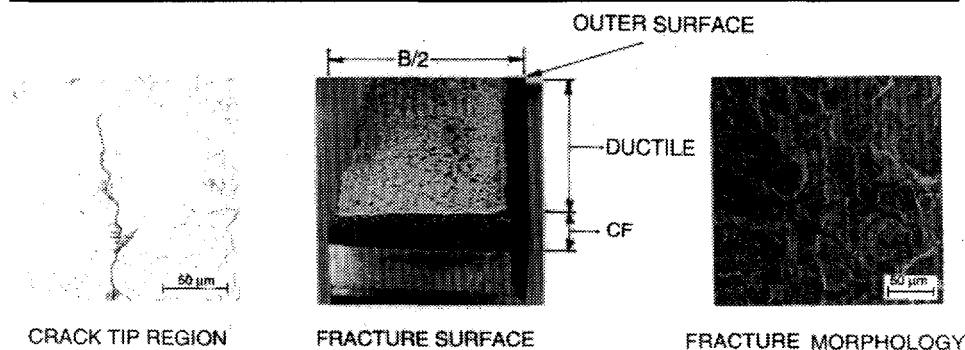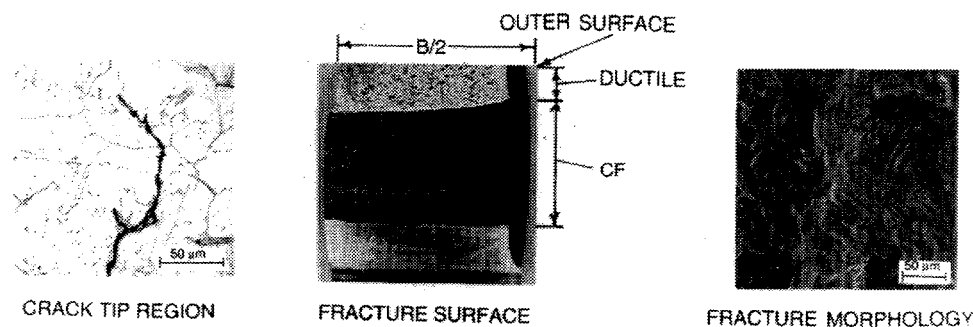*Figure 37. Crack path, fracture surface, and fracture morphology of 1TCT specimen of Alloy 690 (No. HG–09) after crack growth experiment in simulated PWR water at 289 and 320°C*

The Alloy 600 and 690 specimens from the CGR experiments in HP water (Table 8) with a range of DO concentrations and in low–oxygen water with several concentrations of dissolved hydrogen exhibited transgranular modes of crack propagation (Figs. 34 and 35, respectively). The specimens from the CGR experiments in simulated PWR water (Table 9) also revealed predominately transgranular crack propagation (Figs. 36 and 37). The transgranular mode of crack propagation can be attributed to the strong contribution of mechanical cyclic loading in tests at a load ratio of 0.8.

4 Summary and Conclusions

Fracture-mechanics CGR tests were conducted on compact–tension specimens of mill–annealed Alloy 600 and mill–annealed and thermally treated Alloy 690 in oxygenated water and in deoxygenated water that contained boron, lithium, and low concentrations of dissolved hydrogen at 289 and 320°C.

Several tests were conducted on mill–annealed Alloy 600 and sensitized Type 304 SS specimens in simulated BWR water at conductivities of ≈0.08–8.3 $\mu S·cm^{-1}$. Small amounts of chromate and sulfate (<200 ppb) and two amines (1–5 ppm) in water that contained ≈200 ppb DO produced small but measurable changes in the CGRs of the sensitized Type 304 SS specimens but had virtually no effect on the CGR of the mill–annealed Alloy 600 specimen at a load ratio of 0.95. The CGRs of Alloy 600 and sensitized Type 304 SS were virtually the same under conditions where EAC occurred in both materials, i.e., when the stress intensity K exceeded a threshold value at a given load ratio. The average CGR of the Alloy 600 and sensitized Type 304 SS specimens was ≈2.3 x 10^{-10} $m·s^{-1}$ at an R of 0.95 and K_{max} of >30 $MPa·m^{1/2}$ under these water chemistry conditions. This average rate is consistent with numerous determinations of EAC of sensitized Type 304 and nonsensitized Type 316NG SS specimens in oxygenated water at 289°C under similar loading conditions. The observation that different materials, e.g., Alloy 600, sensitized Type 304, nonsensitized Type 316NG, and CF–3, CF–8 and CF–8M grades of cast SSs, exhibit the same CGR in oxygenated water, despite significant differences in material chemistry, microstructure, and mode of crack propagation, suggests that crack propagation is controlled by the rate of cathodic reduction of DO with a concomitant anodic dissolution process at the crack tip. Experimental data for the three

specimens were compared with predictions from an ANL model for CGRs of SSs in water[5] and the ASME Section XI correlation for CGRs in air at the K_{max} and load ratio values in the various tests. The data for both materials were bounded by the two curves.

The crack growth behavior of Alloy 600, Type 316NG, and sensitized Type 304 SS was investigated in simulated PWR water at high load ratios, where an environmental contribution to cracking may be significant. Tests were conducted at 289°C in water that contained 450 ppm boron and 2.25 ppm lithium (added to the feedwater as H_3BO_3 and LiOH), 4–45 cm^3 $H_2 \cdot kg^{-1}$ H_2O, ≈ 1 ppb DO, and 750 ppb hydrazine. The CGR data for the specimens were compared with predictions from the ANL crack–growth model that was modified to account for a very low DO concentration in simulated PWR primary–system water. With the exception of one data point for the Alloy 600 specimen, the experimental results in water were bounded by the ANL model prediction and the "air line" for austenitic SSs from the ASME Code Section XI correlation.

Several CGR tests were performed on this set of specimens in HP water that contained ≈ 6 ppm DO at load ratios between 0.2 and 1.0. CGRs in this environment were also compared with predictions of the ANL model for crack growth in oxygenated water and with the air line from the ASME Section XI correlation at the K_{max} and load ratio values for the specimens. Once again, the experimental data were bounded by the two curves and the ANL model provides a good upper–bound estimate of the CGRs at all load ratios.

Corrosion–fatigue experiments were conducted on mill–annealed Alloy 600 and mill–annealed plus thermally treated Alloy 690 specimens in HP water to investigate the effects of temperature, load ratio, DO, and dissolved hydrogen in water on CGRs. Crack growth behavior of the two materials is quite similar under the conditions in these experiments. At a load ratio of 0.6, the CGRs are not dependent on DO, which is indicative of a strong contribution of cyclic loading to the rates. At a higher load ratio of 0.9, the CGRs decrease as DO concentration decreases at 289 and 320°C. In all cases, the CGRs of both materials lie near or below the air curve for austenitic SSs.

Several tests were conducted at 320°C in HP water that contained <5 ppb DO and ≈ 0, 2.2, and 53 $cm^3 \cdot kg^{-1}$ dissolved hydrogen. At a load ratio of 0.9, CGRs of both specimens were low ($0.5–1.3 \times 10^{-11}$ $m \cdot s^{-1}$) and dissolved hydrogen over the range of $\approx 2–53$ cm^3 $H_2 \cdot kg^{-1}$ H_2O did not influence the rates at a K_{max} of ≈ 34 $MPa \cdot m^{1/2}$. In contrast to results at lower load ratios (i.e., ≤ 0.6), CGRs of Alloy 600 were greater than those of Alloy 690 by factors of $\approx 2–5$.

The influence of dissolved hydrogen in simulated PWR water on CGRs of Alloy 600 and 690 specimens from the same heats of material was determined in another series of experiments at 289 and 320°C. The tests were conducted at a load ratio of 0.8 and K_{max} in the range $\approx 30–39$ $MPa \cdot m^{1/2}$. The CGRs decreased slightly as the dissolved–hydrogen concentration increased from 3 to 58 $cm^3 \cdot kg^{-1}$. Under these water chemistry and loading conditions, CGRs of Alloy 690 were higher by a factor of ≈ 3 than the CGRs of Alloy 600 at both temperatures.

The morphology of corrosion–fatigue cracks in the Alloy 600 and 690 specimens was determined. In simulated BWR water that contained ≈ 200 ppb DO, the crack path in the Alloy 600 and sensitized Type 304 SS specimens was predominantly intergranular. The crack path

in the Alloy 600, Type 316NG, and sensitized 304 SS specimens in which the environment at the beginning and end of the experiment was simulated PWR primary–system water but in which there was an intermediate period of oxygenated HP water, revealed transgranular cracking. Intergranular cracking of the sensitized Type 304 SS specimen in oxygenated water was not observed because of the low load ratios in most of the tests. In deoxygenated HP water and simulated PWR water, predominately transgranular cracking occurred at load ratios <0.9, which were used in most of the tests.

5 Future Work

Corrosion–fatigue tests will be performed on Alloy 600 and 690 specimens with differing heat treatments (Table 1) to assess the influence of microstructure, viz., carbide distribution and grain size, on CGRs in simulated LWR environments. Alloy 690 in the 20% cold–worked condition will also be tested. Most of the experiments will be conducted at R >0.9 to maximize the environmental contribution to crack growth even though CGRs decrease significantly at high load ratios. These tests will confirm whether Alloy 690 exhibits lower CGRs than Alloy 600 at high load ratios, including constant load (R = 1.0). Because CGRs will be relatively low ($<5 \times 10^{-11}$ m·s^{-1}), each experiment will entail a longer test time ($\approx$>800 h) to obtain reliable measurements for incremental crack depths $\approx$>150 μm or several grain diameters. Experiments will be performed in air as well as in water to determine threshold stress intensity values for crack propagation at high R values in both environments. Tests will also be performed over a wider temperature range under conditions where EAC occurs, to quantify the true activation energy for crack propagation. These results will make possible a more quantitative assessment of the degree of environmental enhancement in water for the same material, heat treatment, and loading conditions. The influence of the concentration of dissolved hydrogen in water on crack growth will be investigated at high R values to determine whether there is an abrupt decrease in CGRs over a regime of temperature and hydrogen concentration where the NiO corrosion product is not thermodynamically stable. The results will be compared with similar crack–growth information for austenitic SSs in air from Section XI of the ASME Code and with values predicted by a correlation developed by ANL for EAC of these steels in high–temperature water. If necessary, the correlation will be modified to better reflect the properties of Alloys 600 and 690.
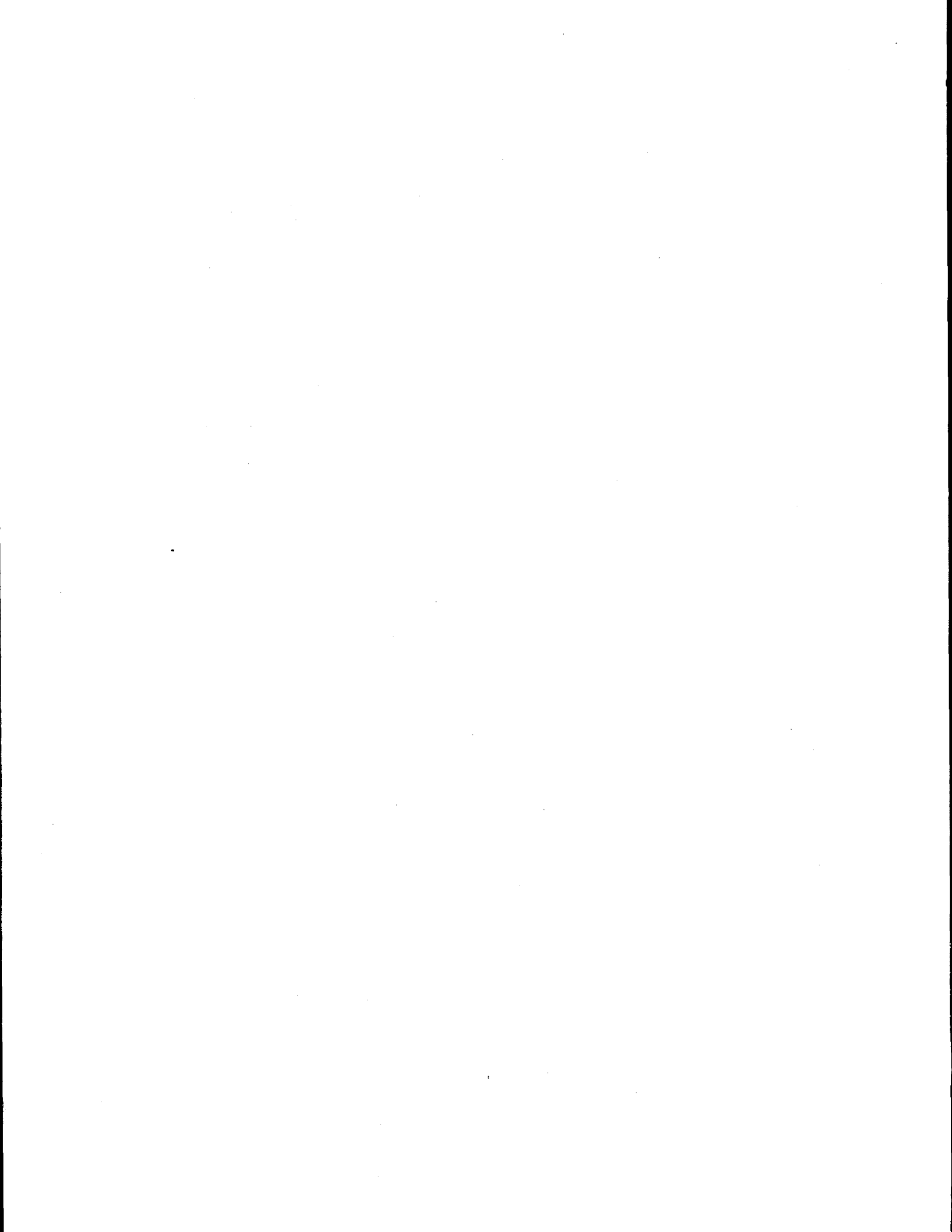
References

1. G. L. Webb and M. G. Burke, *Stress Corrosion Cracking Behavior of Alloy 600 in High Temperature Water*, Proc. 7th Int. Symp. Environmental Degradation of Materials in Nuclear Power Systems – Water Reactors, G. Airey et al., eds., NACE International, Houston, TX, pp. 41–55 (1995).

2. D. A. Mertz, P. T. Duda, P. N. Pica, and G. L. Spahr, *Role of Microstructure in Caustic Stress Corrosion Cracking of Alloy 690*, Proc. 7th Int. Symp. Environmental Degradation of Materials in Nuclear Power Systems – Water Reactors, G. Airey et al., eds., NACE International, Houston, TX, pp. 477–493 (1995).

3. T. M. Angeliu and G. S. Was, *Grain Boundary Chemistry and Precipitation in Controlled Purity Alloy 690*, Proc. 4th Int. Symp. Environmental Degradation of Materials in Nuclear Power Systems – Water Reactors, D. Cubicciotti, ed., NACE, Houston, TX, pp. 5–64 to 5–77 (1990).

4. J. M. Sarver, J. R. Crum, and W. L. Mankins, *Carbide Precipitation and the Effect of Thermal Treatments on the SCC Behavior of Inconel Alloy 690*, Proc. 3rd Int. Symp. Environmental Degradation of Materials in Nuclear Power Systems – Water Reactors, G. J. Theus and J. R. Weeks, eds., The Metallurgical Society, Warrendale, PA, pp. 581–586 (1988).

5. W. J. Shack and T. F. Kassner, *Review of Environmental Effects on Fatigue Crack Growth of Austenitic Stainless Steels*, NUREG/CR–6176, ANL–94/1, (May 1994).

6. W. E. Ruther, W. K. Soppet, and T. F. Kassner, in *Environmentally Assisted Cracking in Light Water Reactors, Semiannual Report, April–September 1994*, NUREG/CR–4667 Vol. 19, ANL–95/25, pp. 20–32 (September 1995).

7. W. E. Ruther, T. F. Kassner, and J. Y. Park, in *Environmentally Assisted Cracking in Light Water Reactors, Semiannual Report, October 1991–March 1992*, NUREG/CR–4667 Vol. 14, ANL–92/30, pp. 33–45 (Aug. 1992).

8. W. E. Ruther and T. F. Kassner, in *Environmentally Assisted Cracking in Light Water Reactors, Semiannual Report, April–September 1993*, NUREG/CR–4667 Vol. 17, ANL–94/16, pp. 22–34 (June 1994).

9. W–K. Lai and Z. Szklarska–Smialowska, *Effect of Heat Treatment on the Behavior of Alloy 600 in Lithiated Water Containing Dissolved Hydrogen at 25 and 350°C*, Corrosion **47**, 40–47 (1991).

10. R. B. Rebak and Z. Szklarska–Smialowska, *Effect of Partial Pressure of Hydrogen on IGSCC of Alloy 600 in PWR Primary Water*, Corrosion **47**, 754–757 (1991).

11. T. F. Kassner, W. E. Ruther, and W. K. Soppet, *Mitigation of Stress Corrosion Cracking of AISI 304 Stainless Steel by Organic Species at Low Concentration in Oxygentaed Water at 289°C*, Corrosion 90, Paper 489, National Association of Corrosion Engineers, April 23–27, 1990, Las Vegas, NV.

12. W. E. Ruther, W. K. Soppet, and T. F. Kassner, in *Light–Water–Reactors Safety Materials Engineering Research Programs:, Quarterly Progress Report, January–March 1985*, NUREG/CR–4490 Vol. 1, ANL–85–75 Vol. 1, pp. 25–42 (March 1986).

13. L. A. James and D. P. Jones, *Fatigue Crack Growth Correlation for Austenitic Stainless Steels in Air*, Proc. Conf. on Predictive Capabilities in Environmentally–Assisted Cracking, R. Rungta, ed., PVP Vol. 99, American Society of Mechanical Engineers, NY, pp. 363–414 (1985).

14. T. Shoji, H. Takahashi, M. Suzuki, and T. Kondo, *A New Parameter for Characterizing Corrosion Fatigue Crack Growth*, J. Eng. Mater. Technol. **103**, 298–304 (1981).

15. J. D. Gilman, R. Rungta, P. Hinds, and H. Mindlan, *Corrosion-Fatigue Crack Growth Rates in Austenitic Stainless Steels in Light Water Reactor Environments*, Int. J. Pressure Vessel Piping **31**, 55-68 (1988).

Distribution for NUREG/CR-6383 (ANL-95/37)

Internal

T. F. Kassner (45)

TIS Files

External

NRC, for distribution per R5

Libraries

    ANL-E (2)

    ANL-W

Manager, Chicago Field Office, DOE

Energy Technology Division Review Committee:

    H. K. Birnbaum, University of Illinois, Urbana

    R. C. Buchanan, University of Cincinnati, Cincinnati, OH

    S. N. Liu, Fremont, CA

    H. S. Rosenbaum, Fremont, CA

    R. K. Shah, University of Kentucky, Lexington

    S. Smialowska, Ohio State University, Columbus

    R. E. Smith, Altran Corporation, Huntersville, NC

P. L. Andresen, General Electric Corporate Research and Development, Schenectady, NY

T. A. Auten, Knolls Atomic Power Laboratory

R. G. Ballinger, Massachusetts Institute of Technology, Cambridge, MA

W. H. Bamford, Westinghouse Electric Corp., Pittsburgh

J. M. Boursier, Electricite de France-Generating and Transmission Group Central Laboratories, Avoine, France

A. Brennenstuhl, Ontario Hydro, Toronto, Ontario, Canada

S. M. Bruemmer, Battelle Pacific Northwest Laboratory

H. S. Chung, Korea Atomic Energy Research Institute, Daejeon, Korea

L. Coressti, ABB CE Nuclear Power, Windsor, CT

R. L. Cowan, General Electric Co., San Jose, CA

G. Cragnolino, Southwest Research Inst., San Antonio, TX

W. H. Cullen, Materials Engineering Assoc., Inc., Lanham, MD

E. D. Eason, Modeling and Computing Services, Newark, CA

J. Fish, Knolls Atomic Power Laboratory

J. P. Foster, Westinghouse Electric Corp., Pittsburgh

M. Fox, Tucson, AZ

D. G. Franklin, Bettis Atomic Power Laboratory

Y. S. Garud, S. Levy, Inc., Campbell, CA
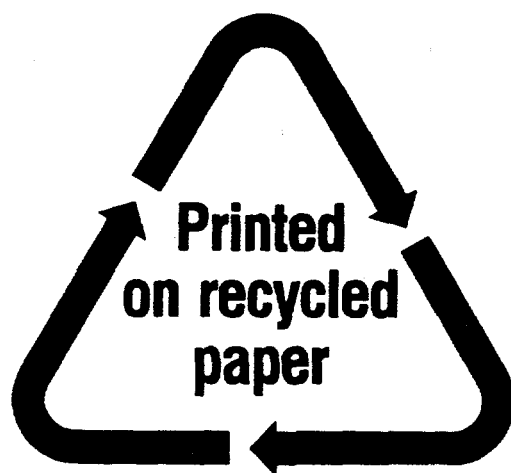
F. Garzarolli, KWU, Erlangen, Germany

J. Gilman, Electric Power Research Inst., Palo Alto, CA

B. M. Gordon, General Electric Co., San Jose, CA

K. Gott, Swedish Nuclear Power Inspectorate, Stockholm, Sweden

M. M. Hall, Bettis Atomic Power Laboratory

J. W. Halley, U. Minnesota, Minneapolis

H. E. Hanninen, Technical Research Centre of Finland, Espoo

D. Harrison, USDOE, Germantown, MD

J. Hickling, CML Capcis March Ltd., Erlangen-Tennonlohe, Germany

M. Higuchi, Ishikawajima–Harima Heavy Industries Co., Ltd., Japan

C. Hoffmann, ABB CE Nuclear Power, Windsor, CT

H. S. Isaacs, Brookhaven National Laboratory

A. Jacobs, General Electric Co., San Jose, CA

L. James, Bettis Atomic Power Laboratory

C. Jansson, Vattenfall Energisystem, Vallingby, Sweden

D. P. Jones, Bettis Atomic Power Laboratory

R. H. Jones, Battelle Pacific Northwest Laboratory

R. L. Jones, Electric Power Research Institute, Palo Alto, CA

T. Karlsen, OECD Halden Reactor Project, Halden, Norway

C. Kim, Westinghouse Electric Corp., Pittsburgh

L. Ljungberg, ABB-ATOM AB, Vasteras, Sweden

D. D. Macdonald, Pennsylvania State University, University Park

T. R. Mager, Westinghouse Electric Corp., Pittsburgh

R. D. McCright, Lawrence Livermore National Laboratory

A. R. McIlree, Electric Power Research Institute, Palo Alto, CA

H. Metha, General Electric Co., San Jose, CA

D. Morgan, Pennsylvania Power and Light Co., Allentown, PA

J. L. Nelson, Electric Power Research Inst., Palo Alto, CA

M. Pytel, Structural Integrity Associates, San Jose, CA

M. Prager, Materials Properties Council, New York, NY

S. Ranganath, General Electric Co., San Jose, CA

P. M. Scott, Framatome, Paris, France

A. J. Sedriks, Office of Naval Research, Arlington, VA

C. Shepherd, AEA Technology–Harwell Labs., Didcot, Oxon, UK

H. D. Solomon, General Electric Corporate Research and Development, Schenectady, NY

M. O. Speidel, Swiss Federal Institute of Technology, Zurich, Switzerland

D. M. Stevens, Lynchburg Research Center, Babcock & Wilcox Co., Lynchburg, VA

P. Tipping, Swiss Federal Nuclear Safety Inspectorate, Villigen, Switzerland

W. A. Van Der Sluys, Research & Development Division, Babcock & Wilcox Co., Alliance, OH

J. C. Van Duysen, Electricite de France-Research and Development Centre de Renardieres, Moret–sur–Loing, France

C. Vitanza, OECD Halden Reactor Project, Halden, Norway

G. S. Was, University of Michigan, Ann Arbor

S. Yukawa, Boulder, CO

U. S. NUCLEAR REGULATORY COMMISSION

BIBLIOGRAPHIC DATA SHEET

(See instructions on the reverse)

1. REPORT NUMBER
(Assigned by NRC. Add Vol., Supp., Rev., and Addendum Numbers, if any.)

NUREG/CR–6383
ANL–95/37

2. TITLE AND SUBTITLE

Corrosion Fatigue of Alloys 600 and 690 in Simulated LWR Environments

3. DATE REPORT PUBLISHED

MONTH	YEAR
April	1996

4. FIN OR GRANT NUMBER

A2212

5. AUTHOR(S)

W. E. Ruther, W. K. Soppet, and T. F. Kassner

6. TYPE OF REPORT

Technical

7. PERIOD COVERED *(Inclusive Dates)*

8. PERFORMING ORGANIZATION – NAME AND ADDRESS *(If NRC, provide Division, Office or Region, U.S. Nuclear Regulatory Commission, and mailing address; if contractor, provide name and mailing address.)*

Argonne National Laboratory
9700 South Cass Avenue
Argonne, IL 60439

9. SPONSORING ORGANIZATION – NAME AND ADDRESS *(If NRC, type "Same as above": if contractor, provide NRC Division, Office or Region, U.S. Nuclear Regulatory Commission, and mailing address.)*

Division of Engineering Technology
Office of Nuclear Regulatory Research
U. S. Nuclear Regulatory Commission
Washington, DC 20555–0001

10. SUPPLEMENTARY NOTES

M. McNeil, NRC Project Manager

11. ABSTRACT (200 words or less)

Crack growth data were obtained on fracture–mechanics specimens of Alloy 600 and 690 to investigate environmentally assisted cracking (EAC) in simulated boiling water reactor and pressurized water reactor environments at 289 and 320°C. Preliminary information was obtained on the effect of temperature, load ratio, stress intensity K, and dissolved–oxygen and –hydrogen concentrations of the water on EAC. Specimens of Type 316NG and sensitized Type 304 stainless steel (SS) were included in several of the experiments to assess the behavior of these materials and Alloy 600 under the same water chemistry and loading conditions. The experimental data are compared with predictions from an Argonne National Laboratory (ANL) model for crack growth rates (CGRs) of SSs in water and the ASME Code Section XI correlation for CGRs in air at the K_{max} and load–ratio values in the various tests. The data for all of the materials were bounded by ANL model predictions and the ASME Section XI "air line."

12. KEY WORDS/DESCRIPTORS *(List words or phrases that will assist researchers in locating this report.)*

Corrosion Fatigue
Crack Growth
Alloy 600
Alloy 690
Types 316NG and 304 Stainless Steel
LWR Environments

13. AVAILABILITY STATEMENT

Unlimited

14. SECURITY CLASSIFICATION

(This Page)

Unclassified

(This Report)

Unclassified

15. NUMBER OF PAGES

16. PRICE